Paleomagnetic determination of emplacement temperatures of pyroclastic deposits: an under-utilized tool

Greig A. Paterson[1], Andrew P. Roberts[1], Conall Mac Niocaill[2], Adrian R. Muxworthy[3], Lucia Gurioli[4], José G. Viramonté[5], Carlos Navarro[6] and Shoshana Weider[2]

[1] National Oceanography Centre, University of Southampton, European Way, Southampton SO14 3ZH, UK. Email: greig.paterson@noc.soton.ac.uk Tel: +44 (0) 23 8059 6478

[2] Department of Earth Sciences, University of Oxford, Oxford OX1 3PR, UK.

[3] Department of Earth Science and Engineering, Imperial College, London SW7 2AZ, UK.

[4] Department of Geology and Geophysics, SOEST, University of Hawaii, 1680 East-West Road, Honolulu, HI 96822, USA.

[5] Instituto Geonorte, Universidad Nacional de Salta, Av. Bolivia 5150–4400, Salta, República Argentina.

[6] Observertorio Vulcanólogico, Universidad de Colima, Av. Gonzalo de Sandoval 444, Colima, Colima CP. 28045, Mexico.

Abstract

Paleomagnetic data from lithic clasts collected from Mt. St. Helens, USA, Volcán Láscar, Chile, Volcán de Colima, Mexico and Vesuvius, Italy have been used to determine the emplacement temperature of pyroclastic deposits at these localities and to highlight the usefulness of the paleomagnetic method for determining emplacement temperatures. At Mt. St. Helens, the temperature of the deposits (T_{dep}) at three sites from the June 12, 1980 eruption was found to be $\geq$532°C, $\geq$509°C, and 510–570°C, respectively. One site emplaced on July 22, 1980 was emplaced at $\geq$577°C. These new paleomagnetic temperatures are in good agreement with previously published direct temperature measurements and paleomagnetic estimates. Lithic clasts from pyroclastic deposits from the 1993 eruption of Láscar were fully remagnetized above the respective Curie temperatures, which yielded a minimum T_{dep} of 397°C. Samples were also collected from deposits thought to be pyroclastics from the 1913, 2004 and 2005 eruptions of Colima. At Colima, the sampled clasts were emplaced cold. This is consistent with the sampled clasts being from lahar deposits, which are common in the area, and illustrates the usefulness of the paleomagnetic method for distinguishing different types of deposit. T_{dep} of the lower section of the lithic rich pyroclastic flow (LRPF) from the 472 A.D. deposits of Vesuvius was ∼280–340°C. This is in agreement with other, recently published paleomagnetic measurements. In contrast, the upper section of the LRPF was emplaced at higher temperatures, T_{dep} ∼520°C. This temperature difference is inferred to be the result of different sources of lithic clasts between the upper and lower sections, with the upper section containing a greater proportion of vent-derived material that was initially hot. Our studies of four historical pyroclastic deposits demonstrates the usefulness of paleomagnetism for emplacement temperature estimation.

Keywords: Emplacement temperature, Mt. St. Helens, paleomagnetism, pyroclastic deposits, Vesuvius, Volcán de Colima, Volcán Láscar.

1 Introduction

Pyroclastic density currents are one of the most deadly volcanic hazards (Tanguy et al. 1998; Witham 2005). Estimating emplacement temperatures for past pyroclastic eruptions helps to quantify risks in regional hazard assessments. The paleomagnetic approach to estimating emplacement temperatures was first suggested by Aramaki and Akimoto (1957), and applied occasionally during the succeeding decades (e.g., Mullineaux and Crandell 1962; Chadwick 1971; Wright 1978). Modifications introduced by Hoblitt and Kellogg (1979), and Kent et al. (1981) led to the method that is used today (McClelland and Druitt 1989; Clement et al. 1993; Bardot 2000; Cioni et al. 2004; McClelland et al. 2004; Porreca et al. 2007; Zanella et al. 2007). The paleomagnetic approach is as follows. During a pyroclastic eruption, explosive fragmentation of juvenile magma breaks up some of the existing volcanic structure and creates a deposit containing fragments of juvenile material and accidental lithic clasts. The accidental lithic clasts will have originally been magnetized prior to the eruption. If a pyroclastic density current was emplaced above ambient temperature, the clasts will have been heated during their incorporation into the deposit and will have then cooled in place after deposition. This heating and cooling will partially or completely reset the magnetization of the clasts. The portion of the magnetization that was reset during the eruption will be aligned with the ambient Earth's magnetic field. This produces two components of magnetization: the original, higher temperature component, which will be randomly oriented for an assemblage of clasts, and a lower temperature component that will consistently align with the Earth's magnetic field at the time of emplacement. Progressive thermal demagnetization can be used to isolate these two magnetization components. The highest temperature at which the low-temperature component is still present provides an estimate of the emplacement temperature of the clast.

2 Paleomagnetic determination of emplacement temperature

The approach outlined above yields the emplacement temperature of each individual clast. It may not represent the temperature reached by the deposit as a whole and it does not take into account the thermal history of the clasts. Clasts that were either cold or hot, prior to eruption, can be incorporated into a single deposit. Clasts that were cold will be initially heated in the deposit, and clasts that were originally hot will cool. There is a temperature at which the deposit will start to cool as a whole; this is identified by the lowest emplacement temperature of the sampled clasts. This temperature is defined as the equilibrium temperature by Bardot and McClelland (2000). Cioni et al. (2004) defined the deposit temperature (T_{dep}) slightly differently. They noted that thin pyroclastic deposits, or clasts that are near the boundaries of the deposit, may experience adverse cooling conditions and that the equilibrium temperature of Bardot and McClelland (2000) may not represent the true temperature of the deposit. Instead, they proposed a temperature estimate based on the overlap of the emplacement temperature of each clast at one locality. They exclude outliers of this overlapping range on the basis of adverse cooling or heating prior to deposition (Cioni et al. 2004; Zanella et al. 2007, 2008). In the case of a thin deposit, the approach of Bardot and McClelland (2000) should underestimate the true temperature of the deposit. Where the sampled deposits are a thermally closed system (i.e., the middle of a thick deposit) both approaches should yield similar results. We use the definition of T_{dep} from Bardot and McClelland (2000) (i.e., the lowest emplacement temperature) to demonstrate the usefulness of paleomagnetism for estimating emplacement temperatures of pyroclastic deposits.

Despite a large published literature on pyroclastics, relatively little work has concentrated on the temperatures of pyroclastic eruptions, with fewer still using paleomagnetism. Paleomagnetism has been used to determine the emplacement temperature

of pyroclastic deposits in 39 published papers (Table 1). The original method proposed by Aramaki and Akimoto (1957) simply involved measurement of the natural remanent magnetization (NRM) of samples without demagnetization. If the NRM direction was consistent with the geomagnetic field at the time of the eruption, the clast was interpreted to have been emplaced hot; if not, then the clast was emplaced cold. Since then the paleomagnetic method of determining emplacement temperatures has been refined to include improved experimental techniques and data analysis. Hoblitt and Kellogg (1979) presented the first paleomagnetic emplacement temperature study to use progressive thermal demagnetization, and Kent et al. (1981) used orthogonal vector component plots (Zijderveld 1967) to separate the recorded paleomagnetic components. Including Kent et al. (1981), only 30 papers have been published using the full demagnetization method (excluding Zlotnicki et al. (1984) who used paleointensities to estimate emplacement temperatures). A number of these papers deal primarily with the magnetic properties of the pyroclastic deposits and only report the emplacement temperatures in passing. Only 19 different localities have been studied. One quarter of the publications are based on data from Santorini, and are primarily from the paleomagnetic group at the University of Oxford. Their work on the extensive deposits of Santorini and the work of the group based at the University of Torino, Italy, represent the only attempts to document the thermal evolution of a pyroclastic volcano and changing emplacement temperatures with changing eruptive styles. Paleomagnetism is therefore an under-utilized tool in volcanology, despite recent efforts by a few groups to use and promote the method. Below, we outline some of the assumptions, potential problems, and advantages of the paleomagnetic method for determining emplacement temperatures with respect to other techniques. We then present results from four volcanoes to highlight the potential and range of applications of the paleomagnetic method.

Table 1

2.1 Non-ideal behaviour

A key assumption behind the paleomagnetic method for estimating emplacement temperatures is that the magnetic remanence acquired at the time of emplacement is a thermal remanent magnetization (TRM) (Bardot and McClelland, 2000; McClelland et al., 2004). Formation of a chemical remanent magnetization (CRM) can affect the blocking temperature spectrum of a sample, and can obscure the emplacement temperature as identified on orthogonal plots of paleomagnetic directions. McClelland et al. (2004) and Porreca et al. (2007) proposed the use of thermomagnetic curves or magnetic susceptibility-temperature curves to detect the possible presence of a CRM. If a Curie temperature of a clast coincides with its apparent emplacement temperature, then the magnetic remanence of the sample could be a CRM. Thermomagnetic measurements can be made rapidly and the most common magnetic mineral to acquire a CRM, maghemite, is readily identifiable on a thermomagnetic curve due to its inversion to hematite or magnetite during heating.

In addition to the possibility of CRM acquisition, the time-temperature dependence of magnetization (Néel, 1949) means that if a clast is exposed to a magnetic field for a prolonged period of time, part of its magnetization will relax and align with the field. This is called a viscous remanent magnetization (VRM). The same VRM can be acquired if the clast is exposed to the same magnetic field for a shorter period of time, but at a higher temperature. This temperature dependence allows VRMs to be removed by thermal demagnetization in the laboratory. A VRM acquired by sampled clasts will record the geomagnetic field between the time of cooling and sample collection. For recent eruptions the VRM direction can be indistinguishable from the paleomagnetic direction acquired by clasts during emplacement. Therefore, the maximum temperature at which a VRM is removed in the laboratory provides a lower limit for emplacement temperature estimates. For a deposit of a given age, there is a minimum emplacement temperature that can be resolved using paleomagnetism. This is determined by the demagnetization temperature required to remove the VRM acquired during longest

period of time that the deposit remains in a constant geomagnetic field. The age-temperature relation for VRM acquisition at ambient temperature (25°C) for common carriers of TRM is shown in Fig. 1.

For example, for clasts containing single-domain (SD) magnetite from a 1 Ma deposit experience the longest period of stable geomagnetic field during the Brunhes Chron (780 kyrs), therefore the minimum emplacement temperature that can be estimated is ∼185°C, for hematite this is ∼290°C. Considering the Curie temperatures of these minerals (580°C and 675°C, respectively) this gives a temperature range of ∼400°C over which emplacement temperature estimates can be made. This extensive age range demonstrates the distinct advantage of the paleomagnetic method over other approaches.

Fig. 1

Another potential source of non-ideal behaviour arises from the presence of multidomain (MD) grains. When a magnetic grain grows large enough the magnetization no longer remains uniform as for SD grains and the magnetization is divided up into regions (domains) of varying magnetization. Such grains have non-ideal paleomagnetic behaviour (e.g., Bol'shakov and Shcherbakova 1979; Shcherbakova et al. 2000; Fabian 2003), particularly with respect to paleointensity studies (e.g., Levi 1977). The remanence acquired by MD grains does not unblock at the same temperature at which it was blocked, which produces what is known as a partial TRM (pTRM) tail (i.e., a portion of magnetic remanence that demagnetizes above the acquisition temperature; Bol'shakov and Shcherbakova 1979). Such tails can commonly only be removed by demagnetization to the Curie temperature. The presence of a pTRM tail produces an overlap in the unblocking temperature spectra of different magnetization components in a sample, which will be evident as curvature on the vector component diagram. If only a single component of magnetization is present, the overlapping blocking temperatures will record the same direction, and the paleomagnetic directional analysis will be unaffected. The presence of MD grains will therefore not compromise paleomagnetic emplacement temperature estimates.

3 Other methods for determining emplacement temperatures

Estimates of the emplacement temperature for a pyroclastic deposit can be made directly using a thermal probe or remotely, by satellite. Relatively few direct measurements have been published (e.g., Banks and Hoblitt 1981; Cole et al. 1998; Calder et al. 1999; Druitt et al. 2002), largely because of the risk associated with visiting an active volcanic region shortly after an eruption. Satellite observations using Advanced Very High Resolution Radiometer (AVHRR) imagery provide excellent spatial resolution, but are only capable of measuring temperatures up to ∼250°C (Denniss et al. 1998).

Field evidence provides another means of studying the thermal history of a pyroclastic deposit. Features such as gas escape pipes, vesicles within the ash matrix, carbonized materials and discolouration of lithic fragments provide evidence of high temperature emplacement. However, these features are often not present or visible and do not always allow quantitative estimation of emplacement temperature. Other, more quantitative, methods have also been used. These include oxidation colours of pumice (Tsuboi and Tsuya 1930), infra-red spectroscopy of wood fragments (Maury 1971), and analysis of bone fragments (Capasso et al. 2000). Voight and Davis (2000) used the melting points of plastic bottles to estimate the emplacement temperatures of pyroclastic deposits at Merapi Volcano, Java, Indonesia. This novel approach has limited usefulness and only allows temperature estimates up to ∼150–250°C. Sawada et al. (2000) investigated use of the H/C ratio of carbonized wood as a paleo-thermometer. Controlled laboratory experiments and analysis were used to show that the correct heating temperature is recoverable with this method. When applied to Holocene pyroclastics, the H/C ratio method gave results that were consistent with paleomagnetic data (Sawada et al. 2000).

4 Sampling and experimental procedures

Several localities were studied here to demonstrate the widespread usefulness of the paleomagnetic method for determining emplacement temperatures of pyroclastic deposits. At all localities sampled in this study, oriented hand specimens were collected using the method described by Tarling (1983). A horizontal line was marked, on a relatively flat surface, on each clast. The strike of this line and the dip of the surface were measured using a magnetic compass-clinometer. Cores with a diameter of 10 or 20-mm were then drilled from the clasts in the laboratory. Remanence measurements were made within a magnetically shielded laboratory using either a 2-G Enterprises cryogenic magnetometer, or a Molspin Minispin magnetometer at the University of Southampton or at the University of Oxford. Thermal demagnetization was carried out at 20-50°C steps using either an ASC Scientific or a Magnetic Measurements thermal demagnetizer, both of which have residual fields of less than 50 nT. Following every heating step, the low-field magnetic susceptibility was measured at room temperature to check for signs of thermal alteration, using an Agico KLY-4S Kappabridge or a Bartington Instruments MS2B magnetic susceptibility meter. Additional sister samples were cut for rock magnetic measurements using a Princeton Measurements Corporation Vibrating Sample Magnetometer (VSM) at Southampton (maximum field of 1 T) and using an Agico KLY-2 Kappabridge magnetic susceptibility meter with furnace attachment at Oxford. Thermomagnetic curves were analysed using the RockMag Analyzer software (Leonhardt 2006), and susceptibility-temperature curves were analysed using the inverse susceptibility method outlined by Petrovský and Kapička (2006).

5 Results

5.1 Mt. St. Helens, USA

Mt. St. Helens is located in the Cascade Mountain Range of the western U.S.A., and is famous for its devastating eruption on May 18, 1980. This eruptive phase began in

late March of 1980 with a series of generally short-lived eruptions. A magnitude 5.1 earthquake on May 18 triggered a landslide that caused rapid depressurization of the northern flank of the volcano, which triggered a lateral surge cloud. Activity continued at Mt. St. Helens during 1980 and the collapse of eruptive columns generated numerous pyroclastic density currents and deposits (Smithsonian Institution 1980). Within days to weeks of the pyroclastic deposits being emplaced, direct temperature measurements were taken by a group from the United States Geological Survey (Banks and Hoblitt 1981). The full procedure and emplacement temperature analysis was presented by Banks and Hoblitt (1996). The debris avalanche was emplaced at low temperatures (<100°C), while the lateral blast deposit was emplaced at slightly higher temperatures (100–200°C). The pyroclastic deposits were much hotter, and were emplaced at 300°C to >600°C (Banks and Hoblitt 1996). Although the sites sampled in this study do not coincide exactly with those of Banks and Hoblitt (1996), the measured temperatures have been extrapolated based on the available data of Banks and Hoblitt (1996) and compared with our paleomagnetically determined temperatures.

A total of 113 clasts were collected from 6 different sites on the northern flank of Mt. St. Helens (Fig. 2). The lithic clasts include basalts, andesites and dacites. Thermal demagnetization up to around 125°C will remove potential viscous magnetizations, so low temperature steps are excluded from analysis of the recorded paleomagnetic directions. The measured samples have both single and multiple components of magnetic remanence (Fig. 3).

Fig. 2

Sites MSH1 and 2 do not record a well-defined paleomagnetic direction (Fig. 4). Samples with two components of remanence indicate emplacement temperatures in the 330–390°C temperature range. Direct measurements by Banks and Hoblitt (1996) give the temperature of the May 18 deposits in this area to be ∼300–367°C. It seems most likely that the scattered paleomagnetic directions for these clasts therefore result from localized reworking and do not result from low temperature pyroclastic emplacement.

Fig. 3

Sites MSH3, 5 and 6 all have well-defined paleomagnetic directions that record the

Fig. 4

expected geomagnetic field direction during 1980 (Fig. 4). Site MSH4 also records this direction, but it is poorly defined. However, the statistic $3R^2/N$, which provides a test for randomness (Rayleigh 1919), indicates that the paleomagnetic directions are statistically grouped at the 95% confidence level. The statistic will exceed 7.81 for a group of non-random paleomagnetic directions; the statistic at sites MSH3-6 exceeds 7.81. At both sites MSH1 and 2, $3R^2/N$ is $\leq$5.9, which indicates that no consistent paleomagnetic direction is recorded.

Sixty-two samples from sites MSH3–6 have paleomagnetic directions that fall within 30° of the 1980 geomagnetic field direction. These samples were used to determine emplacement temperatures. The majority of samples have single components of magnetization, which means they were emplaced above the Curie temperature (T_c) of the constituent magnetic minerals. Curie temperatures of the clasts (Fig. 5a, b and Table 2) are 447–634°C for the juvenile material, and 460–634°C for the lithic clasts.

Fig. 5

Table 2

Sites MSH3, 5 and 6 are all from the deposits emplaced on June 12, 1980. Extrapolation from the data of Banks and Hoblitt (1996) give emplacement temperature at these three sites of around 540 ± 30°C. At site MSH3, the June 12 deposits were rich in hot ($\geq$447–595°C) juvenile material. The sampled lithic clasts were emplaced at or above T_c. T_{dep} can only be constrained to have been hotter than the lowest T_c; for site MSH3 T_{dep} $\geq$532°C. This is in good agreement with the direct measurements of Banks and Hoblitt (1996) (Fig. 6). At site MSH 5, where the juvenile content is lower, the lithic clasts also record only one paleomagnetic direction. The T_c of these clasts is 509–619°C. T_{dep} at MSH5 was $\geq$509°C. All but one sample at site MSH6 have single components of magnetization. The Curie temperatures of the lithic samples are 527–634°C. Sample MSH6C1 records two paleomagnetic directions. The intersection of these two directional components gives an emplacement temperature of 510–570°C. Although only one sample gives this result, it is considered to provide an accurate estimate of T_{dep}. We exclude the possibility of adverse cooling of this particular clast as it was sampled from a similar level within the deposit as clasts emplaced at temperatures

above T_c, and so will have experienced the same cooling conditions. A paleomagnetic estimate of T_{dep} = 510–570°C is in excellent agreement with the measured value from Banks and Hoblitt (1996) of 540 ± 30°C (Fig. 6).

Fig. 6

The deposit at site MSH4 was emplaced on July 22, 1980, and direct measurements by Banks and Hoblitt (1996) give an emplacement temperature of >600°C. The sampled clasts all have single components of magnetization. T_c for the lithic clasts range from 577 to 603°C, and for the juvenile material from 623 to 634°C. T_{dep} is taken to be ≥577°C. This estimate also agrees with the measurements of Banks and Hoblitt (1996) (Fig. 6).

Paleomagnetic emplacement temperatures of Erwin (2001) along with the new data presented here, and those of Sulpizio et al. (2008) from El Chichón, Mexico are plotted against available directly measured emplacement temperature data in Fig. 6. These data illustrate the accuracy of the paleomagnetic method for estimating emplacement temperatures of pyroclastic deposits and highlight the repeatability of paleomagnetic measurements.

5.2 Volcán Láscar, Chile

Láscar is a stratovolcano in the Chilean Andes, near the Argentinean border (Fig. 7a). On April 18, 1993, Láscar erupted for three days, in what was the largest historic eruption in the northern Andes (Smithsonian Institution 1993; Déruelle et al. 1995, 1996). Two intense eruptions on April 19 produced ejecta columns as high as 22 km. Pyroclastic density currents resulted on April 19 and 20 following the collapse of eruptive columns. The pyroclastic deposits crop out on the volcano flanks up to 8.5 km from the summit toward the NW and SE (Fig. 7a) and cover an area of ∼18.5 km^2.

Fig. 7

The deposits contain a pumice-rich facies typically found in the frontal lobes and margins of the deposits and a lithic-rich facies in the interior of the deposits (Sparks et al. 1997). The pumice facies comprises an andesitic-dacitic juvenile component with a minor lithic content. The lithic-rich facies incorporates roughly equal proportions

of eroded and vent-derived lithic clasts. These include fragments of the pre-existing andesitic lava dome, formed in 1992, and clasts from the Tumbres-Talabre lava. Clasts of Tertiary ignimbrite and pink quartz rhyodacite were also incorporated, although they are not common (Déruelle et al. 1996; Sparks et al. 1997; Calder et al. 2000).

No direct temperature measurements of the pyroclastic deposits were made; however, due to its high altitude (5.5 km above sea level) and reduced cloud cover, Láscar is ideal for satellite observations (Oppenheimer et al. 1993; Wooster and Rothery 1997; Denniss et al. 1998; Wooster et al. 1998; Wooster 2001). Denniss et al. (1998), using AVHRR satellite imagery, produced a thermal radiance map of the 1993 Láscar pyroclastic deposits (Fig. 7b). Their results indicate a central hot area associated with the volcanic vent. The distinct shape of the northern deposits is also evident as areas with elevated temperatures. The southern slopes of Láscar were obscured by the ash plume, so no temperature estimates are available for these deposits. The available satellite data indicate that the minimum surface temperature of the deposits was ∼185–265°C. It must be noted this is the maximum temperature range that can be estimated using AVHRR imagery, so this range provides a minimum estimate of emplacement temperature for the pyroclastic density currents.

A total of 111 clasts, representing 31 sites from pyroclastic deposits on both flanks of Láscar, were collected. The sampled lithic clasts are andesitic to dacitic in composition. Little erosion had occurred at Láscar between the eruption in 1993 and our sampling during early 2006. We could therefore only sample the presently exposed surface of the deposits. Thermal demagnetization was performed on 124 samples cut from the clasts. Two main types of demagnetization behaviour are evident (Fig. 8). Most of the samples have a single magnetization component that is aligned with the 1993 geomagnetic field direction (Fig. 8a). An additional 18 samples, from dacitic clasts, provide evidence of self-reversing behaviour; the high temperature component is consistent with the 1993 geomagnetic field direction, but the lower temperature component is anti-parallel to this direction (Fig. 8b). The 1993 geomagnetic field direction is present up to the Curie

temperature of these samples, which indicates that the clasts were fully remagnetized during the 1993 eruption.

Fig. 8

Fig. 9a is a stereoplot of the recorded paleomagnetic directions; the paleomagnetic directions are biased toward the 1993 geomagnetic field direction and its antipode. Fig. 9b is a stereoplot of the recorded paleomagnetic directions that fall within 30° of the 1993 geomagnetic field direction; these clasts are used to estimate the emplacement temperature. Of the samples with self-reversing magnetizations, 17 have well-defined normal and reverse polarity components of magnetization (with maximum angular deviation, MAD $\leq 15°$). A further 11 samples have well-defined high temperature, normally magnetized components but have poorly defined (MAD $> 15°$) low temperature components of magnetization, which fall close to the antipodal direction of the 1993 geomagnetic field. Due to their high MAD values, these low temperature components of magnetization are excluded from further analysis. A reversal test for the two, well-defined directions (Fig. 9c) yields overlapping α_{95} cones of confidence, which indicates that the directions are antipodal. The reversal test of McFadden and McElhinny (1990) yields an angular separation, γ_0, of 5.7°, and a critical angle, γ_c, of 6.5°. This constitutes a positive reversal test ($\gamma_0 < \gamma_c$) of quality classification 'B' ($5° < \gamma_c \leq 10°$).

Fig. 9

A total of 80 samples (72 independent clasts) unambiguously recorded the Earth's magnetic field during the 1993 eruption, which includes samples from 30 of the 31 sites sampled. The paleomagnetic data for the normal polarity component closely cluster around the ambient field direction during April 1993 (Fig. 9a, b). The paleomagnetic inclination is shallower by a few degrees; this inclination error is most likely caused by clast rotation during compaction of the deposits, as suggested by Hoblitt et al. (1985).

Each clast indicates emplacement temperatures in excess of T_c (Table 3). Thermomagnetic curves (Fig. 5c, d) yield T_c values from 397°C to 641°C, while T_c of the juvenile material ranges from 402°C to 599°C. Although there is no lowest emplacement temperature on which to base an estimate of T_{dep}, the uniformly high temperature of

both the juvenile material and the lithic clasts suggests a high T_{dep} value ($\geq$397°C).

Table 3

Despite the consistently high emplacement temperatures at nearly all of the sampled sites, 9 samples yielded noisy data and failed to record the 1993 geomagnetic field direction. These samples were not included in any further analysis. Another 35 samples do not record consistent paleomagnetic directions. This normally indicates cold emplacement. At each site, however, samples were collected from within a limited area and the distance between samples was typically less than 5 m. This suggests implausible temperature gradients within the deposit if some samples were emplaced cold and others hot. A much more likely scenario is that these samples have moved since they cooled. This interpretation is supported by the fact that only the surface of the deposit could be sampled.

5.3 Volcán de Colima, Mexico

The Colima Volcanic Complex, located in western Mexico, is a N-S trending volcanic chain consisting of three volcanoes: Volcán Cantaro, Nevado de Colima and Volcán de Colima (Fig. 10). Volcán de Colima is currently Mexico's most active volcano with at least 52 eruptions since 1560 A.D. (Bretón et al. 2002). Intermittent activity has been observed since 1998, with vulcanian eruptions, lava flows and growing domes that have collapsed and generated pyroclastic density currents (Saucedo et al. 2002; Zobin et al

Fig. 10

2002; Saucedo et al. 2004, 2005).

Thirteen localities were sampled from areas where pyroclastic eruptions occurred on June 2005 (VC1–7), January 1913 (VC8–11), and June 2004 (VC12-13). Two areas associated with the 2005 deposits were sampled where pyroclastic emplacement was observed, in the northern end of Montegrande gully (VC1–4), and further east in La Arena gully (VC5–7). Sites VC8–11 were located in the northern end of Zarco river valley, and samples from the 2004 deposits (VC12–13) were collected from the western flank of the volcano inside the Rio la Lumbre river valley. Thermal demagnetization was carried out on 133 samples from 107 clasts, which reveals both single and multiple

magnetization components (Fig. 11a). A stereographic projection of all of the low temperature paleomagnetic components, which includes single remanence components, is shown in Fig. 11b. Only one of the paleomagnetic directions falls close to the geomagnetic field direction during the respective eruptions that produced the sampled deposits (indicated by the two stars). The test for randomness is not satisfied ($3R^2/N = 38.2$), which suggests a bias in the recorded directions toward a downward and southeastward direction, although no statistically reliable direction can be identified (Fig. 11b). The recorded paleomagnetic directions all have low MAD values, which indicates that the scatter of directions is not simply due to noise (Table 4). The lack of a contemporaneous geomagnetic field direction indicates that the sampled clasts were emplaced in their current deposits below the temperature at which the viscous overprint is removed, i.e., below ∼115°C for the 2004/5 deposits and below ∼135°C for the 1913 deposits. The wet local climate means that pyroclastic debris is frequently remobilized as lahars, often soon after an eruption (Davila et al. 2007). Therefore, the most probable explanation of the data distribution is that the sampled deposits represent reworked pyroclastics. The presence of numerous clasts with two components of magnetic remanence may suggest that the clasts have undergone reheating/remagnetization at some point in the past, which supports the hypothesis that the clasts are most likely sourced from pyroclastic deposits. The wide range of potential emplacement temperatures indicated by these multicomponent clasts (250–450°C) provides little information about the emplacement temperature of the reworked deposits because there is no constraint on the origin of the clasts (i.e., they could be sourced from numerous deposits with varying emplacement temperature).

Fig. 11

Numerous pieces of charred wood and plant debris are visible within the sampled deposits. The presence of these fragments suggests that the deposits were emplaced above ambient temperature, while the paleomagnetic evidence indicates that the deposits were emplaced at ambient temperature. The possibility of accessory materials being reworked into cold deposits and giving rise to false emplacement temperature

Table 4

estimates highlights the value of the paleomagnetic method for determining pyroclastic emplacement temperatures.

5.4 Vesuvius, Italy

Numerous investigations have been made of the temperature from the 79 A.D. eruption of Vesuvius using both paleomagnetic (e.g., Kent et al., 1981) and non-paleomagnetic methods (e.g., Mastrolorenzo et al., 2001). Kent et al. (1981), in their pioneering work on developing the paleomagnetic method, investigated lithic fragments and juvenile material from pyroclastic deposits in the town of Herculaneum. Their results suggest that the deposits could not have been hotter than ∼400°C. Both Capasso et al. (2000) and Mastrolorenzo et al. (2001) analysed bone fragments from the bodies of victims killed by the pyroclastics at Herculaneum. Capasso et al. (2000) estimated that the bones reached temperatures of up to 350–400°C, while Mastrolorenzo et al. (2001) suggested higher temperatures of ∼500°C. Mastrolorenzo et al. (2001) also used paleomagnetism to investigate a tile fragment, estimating its emplacement temperature to be 480°C. Cioni et al. (2004), using paleomagnetism, investigated the temperature of the pyroclastic deposits on a much wider scale, and sampled 13 sites around the volcano. Their results indicate that the pyroclastics were emplaced at temperatures of 180–380°C. Zanella et al. (2007) investigated the temperature of the 79 A.D. deposits at Pompeii in detail. These deposits reached temperatures up to 320°C, but were as cool as 180°C in some areas. This variation of a few hundred degrees over short distances illustrates the effect that urban areas can have on the temperature of pyroclastics and might explain the temperature variations documented at Herculaneum. Zanella et al. (2008) recently investigated the 472 A.D. deposits from Vesuvius. These deposits were uniformly hot with T_{dep} ∼260–360°C irrespective of locality and the facies sampled. They concluded that the uniformity of deposit temperature can be attributed to similar rates of heat transfer from juvenile to lithic clasts and/or to similarity in deposition regimes of the different facies. Based on the similar temperatures from both phreatomagmatic

and magmatic facies, they also concluded that magma-water interactions had little influence on T_{dep}.

At our sampled locality, Pollena quarry (Fig. 12), Cioni et al. (2004) estimated the emplacement temperature of the 79 A.D. pyroclastics to be 250–310°C, while Zanella et al. (2008) estimated the 472 A.D. deposits to have been emplaced at 280–320°C. We sampled 124 lithic clasts from the 472 A.D. deposits at the Pollena quarry, on the western flank of Vesuvius (Fig. 12). Six sites were sampled from the lithic rich pyroclastic flow (LRPF) and the F_g facies described by Sulpizio et al. (2005, 2007). The sampled clasts are predominantly leucite-bearing tephrites, with occasional andesites and a syenite (Table 5). Any VRM should be removed by laboratory heating to ∼150°C, therefore data below this heating step are ignored.

Fig. 12

Three main types of remanence behaviour are identified, with most samples having a single magnetization component (Fig. 13a). A number of samples have more complicated, multi-component magnetizations (Fig. 13b, c). Equal area stereographic projections of the low temperature magnetization components recorded at the six sampled sites are shown in Fig. 14. There is no consistency in the paleomagnetic directions at site CP1. Evidence of debris flows at this site raised doubts when sampling as to whether the site was *in-situ*; the paleomagnetic data confirm that these samples have been remobilized. At sites CP3–6 the paleomagnetic directions are biased toward a northward and downward direction. Only 3 samples were available from site CP2, but the same trend is still identifiable. At each of these sites, $3R^2/N$ exceeds 7.81 (Fig. 14), which indicates that the paleomagnetic directions are statistically grouped. A mean paleomagnetic direction was obtained by grouping sites CP2–6 (Dec. = 352.6°, Inc. = 57.1°, α_{95} = 8.5°, N = 95, R = 70.9, k = 3.9, $3R^2/N$ = 158.6). This direction is consistent with paleomagnetic directions recorded in previous studies (e.g., Tanguy et al. 2003; Zanella et al. 2008). To isolate clasts that record a consistent direction, data from sites CP2–6 were excluded if the paleomagnetic direction was >30° away from the mean paleomagnetic direction. A total of 63 clasts were thereby used to estimate

Table 5

Fig. 13

emplacement temperatures. At least 3 clasts from each site met this selection criterion.

Fig. 14

Thermomagnetic analysis was carried out on all of these clasts (e.g., Fig. 5e, f). Sample CP4Q has a Curie temperature that coincides with its estimated emplacement temperature (Fig. 5e). This might be because the sample has a CRM, therefore it was excluded from further analysis. Sample CP6Q has behaviour that is typical of the inversion of maghemite to hematite (Fig. 5f). This is strong evidence that maghemite is the main magnetic mineral and that the magnetic remanence of this lithic clast is a CRM. This sample was also removed from further consideration.

The three clasts from site CP2 (from the F_g facies) were remagnetized above the Curie temperature of their constituent magnetic minerals. T_c values range from 568 to 580°C (Table 5). The small number of samples precludes a reliable estimate of the deposit temperature at this locality. Sites CP3 and 4 are from the lower 2 m of the exposed LRPF within Pollena quarry. Variable emplacement temperatures were estimated from ∼280°C to above T_c. The majority of clasts have multi-component remanences, which indicate emplacement between 310 and 460°C. The deposit temperature is constrained by the lowest temperature experienced by an individual clast. For site CP3, T_{dep} = 310–340°C, and T_{dep} = 280–340°C for site CP4. T_{dep} of the lower section of the LRPF is 280–340°C. This agrees well with the estimate of Zanella et al. (2008) of T_{dep} = 280–320°C. This result emphasizes the inter-laboratory repeatability of the paleomagnetic method. Sites CP5 and 6 are from the upper part of the LRPF. The majority of clasts from these sites were emplaced above T_c, but three clasts from site CP5 and two clasts from site CP6 were emplaced at ∼520°C. Curie temperatures at these two sites range from 533 to 649°C. T_{dep} is taken to be ∼520°C. This estimate is higher than the 280–320°C estimated by Zanella et al. (2008). The temperature contrast between the upper and lower LRPF and the data of Zanella et al. (2008) is large (∼200°C). Few samples measured by Zanella et al. (2008) have single magnetization components that indicate full remagnetization of clasts (∼1%); similarly, in this study the lower

LRPF has relatively few fully remagnetized clasts. This suggests that the majority of clasts incorporated into this part of the deposit experienced little or no heating prior to deposition. In contrast, the upper section of the LRPF sampled in this study predominantly contains clasts that have been remagnetized above T_c. This suggests that these clasts have undergone considerable heating before deposition. From this we infer that the upper and lower sections of the LRPF have different sources of lithic clasts. The clasts from the lower LRPF are sourced from the cold debris on the flanks of the volcano, while clasts from the upper LRPF are most likely to be vent-derived lithics that were initially hot.

6 Discussion

Determining the emplacement temperature of pyroclastic deposits can aid in the assessment of volcanic hazards. Establishing the thermal evolution of an eruptive phase or the entire thermal history of a volcano can help to refine predictions of hazards associated with future activity. Paleomagnetism provides an under-utilized tool for such studies. We have used paleomagnetism to investigate the emplacement temperatures of pyroclastic deposits from historic eruptions of four volcanoes. Mt. St. Helens, USA, provides an ideal locality to test the paleomagnetic method against direct measurements taken shortly after deposition. Erwin (2001) highlighted the accuracy of the paleomagnetic method at Mt. St. Helens. We provide additional data, which further confirms the usefulness of the paleomagnetic method. Our analysis of clasts and juvenile material collected from the June and July 1980 pyroclastic deposits confirm the paleomagnetic determinations of Erwin (2001) and agrees well with the direct measurements of Banks and Hoblitt (1996). The three sampled localities of the June 1980 pyroclastics (MSH3,5 and 6) were emplaced $\geq$532°C, $\geq$509°C and at 510–570°C. For the July 1980 pyroclastics (MSH4), T_{dep} $\geq$577°C.

At Láscar, Chile, paleomagnetic data also indicate that the clasts were emplaced above T_c at $\geq$397°C. Satellite imagery provides an estimate of T_{dep} $\geq$185–265°C (Den-

niss et al. 1998). Satellite methods do not allow higher temperature estimates, so paleomagnetic determinations have proven more useful in this case. The presence, and inclusion, of samples that exhibit self-reversing behaviour may give rise to uncertainties with these estimates. Alternating field demagnetization data confirm that the NRM of the samples in question is affected by self-reversal, which indicates that the self-reversing mechanism occurred naturally and that it is not an artefact of thermal demagnetization. If we consider the directions recorded by the self-reversing and non-self-reversing samples independently, we can perform a statistical analysis to test if the two directions are distinguishable (e.g., Butler 1992). The F-statistic indicates that the two directions cannot be distinguished at the 95% confidence level, where $F = 0.332 << 3.054$ (the critical F value for the two datasets).

At Colima, Mexico, the opposite end of the spectrum is observed, where the sampled clasts were cold when emplaced into their current deposits. This suggests that the sampled deposits most likely represent lahars. This illustrates the usefulness of paleomagnetism for discriminating between different types of deposits, which is useful when differentiation based on field or satellite observations is difficult.

Results from Vesuvius, Italy, highlight the potential of the paleomagnetic method to investigate the emplacement temperature of older deposits. Emplacement temperatures of the individual clasts range from ∼280°C to above T_c (∼533–649°C). The deposit temperature was ∼280–340°C for sites CP3 and CP4 (lower section of the LRPF), and ∼520°C for sites CP5 and CP6 (upper section of the LRPF). Few samples from sites CP5 and CP6 have two magnetization components, which suggests that the deposit was emplaced close to T_c. We attribute the higher emplacement temperature recorded from the lower LRPF compared to the upper LRPF to changes in the source of lithic material. The lower LRPF contains initially cold lithic clasts, while the upper section contains initially hot clasts that were most likely sourced from or close to the volcanic vent.

7 Conclusions

This study highlights a number of key advantages in using the paleomagnetic method to determine the emplacement temperature of pyroclastic deposits.

1. The paleomagnetic method is as accurate as directly measuring temperatures shortly after deposition. Paleomagnetic sampling has the added benefit of not having to visit an active volcanic region immediately after an eruption.

2. The method is repeatable between laboratories, which allows reliable comparisons between different measurements.

3. Paleomagnetism provides a wide temperature range for estimating emplacement temperatures, up to 580–675°C, depending on the magnetic minerals present.

4. The method has a much wider emplacement temperature range than can be determined from satellite data and can be applied in the absence of materials such as wood or man-made materials, which may not always be present.

5. The presence of charred materials in reworked deposits provides ambiguity that can be resolved with paleomagnetism, which highlights the possibility that such proxies may give inaccurate emplacement temperature estimates.

6. The paleomagnetic method can be used to investigate emplacement temperatures over long time scales. Stable recordings of the geomagnetic field can be carried by single domain magnetic grains over billions of years. This contrasts with direct measurements that are limited to recent and future events. Man-made materials are only available over the past several thousand years, and useful charred wood fragments are unlikely to survive over long time scales.

Acknowledgments

This study was funded by NERC grant NER/S/A/2005/13478. Collection of the Mt. St. Helens, Colima and Vesuvius samples was funded through a Royal Society grant to ARM. We thank Karen Paola Guzmán Montenegro for assistance with collecting samples from Láscar, Jose Guadalupe Landin Orozco for assisting with sampling at Colima and Francesca Lawley and Andrew Harris for assistance at Vesuvius. We thank Michelle Harris for assistance with lithology classification. We also thank two anonymous reviewers for their helpful comments that improved the manuscript.

References

Alva-Valdivia LM, Rosas-Elguera J, Bravo-Medina T, Urrutia-Fucugauchi J, Henry B, Caballero C, Rivas-Sanchez ML, Goguitchaichvili A, Lopez-Loera H (2005) Paleomagnetic and magnetic fabric studies of the San Gaspar ignimbrite, western Mexico - constraints on emplacement mode and source vents. J Volcanol Geotherm Res 147:68–80 DOI 10.1016/j.jvolgeores.2005.03.006

Aramaki S, Akimoto S (1957) Temperature estimation of pyroclastic deposits by natural remanent magnetism. Am J Sci 255:619–627

Banks NG, Hoblitt R (1981) Summary of temperature studies of 1980 deposits. In: Lipman PW, Mullineaux DR (eds) The 1980 Eruptions of Mount St. Helens, Washington. USGS Professional Paper 1250:295–313

Banks NG, Hoblitt RP (1996) Direct temperature measurements of deposits, Mount St. Helens, Washington, 1980–1981. USGS Professional Paper 1387

Bardot L (2000) Emplacement temperature determinations of proximal pyroclastic deposits on Santorini, Greece, and their implications. Bull Volcanol 61:450–467. DOI 10.1007/PL00008911

607 Bardot L, McClelland E (2000) The reliability of emplacement temperature estimates
608 using palaeomagnetic methods: a case study from Santorini, Greece. Geophys J Int
609 143:39–51 DOI 10.1046/j.1365-246x.2000.00186.x

610 Bardot L, Thomas R, McClelland E (1996) Emplacement temperatures of pyroclastic
611 deposits on Santorini deduced from palaeomagnetic measurements: constraints on
612 eruption mechanisms. In: Morris A, Tarling DH (eds) Palaeomagnetism and tectonics
613 of the Mediterranean region. Geol Soc London Spec Pub 105:345–357

614 Bol'shakov, AS, Shcherbakova VV (1979) Thermomagnetic criterion for determining the
615 domain structure of ferrimagnetics. Izv Acad Sci USSR Phys Solid Earth 15:111–117

616 Bretón M, Ramírez JJ, Navarro C (2002) Summary of the historical eruptive activity
617 of Volcán De Colima, Mexico 1519–2000. J Volcanol Geotherm Res 117:21–46 DOI
618 10.1016/S0377-0273(02)00233-0

619 Butler, RF (1992), Paleomagnetism: Magnetic Domains to Geologic Terranes. Blackwell
620 Scientific Publications, Boston

621 Calder ES, Cole PD, Dade WB, Druitt TH, Hoblitt RP, Huppert HE, Ritchie L, Sparks
622 RSJ, Young SR (1999) Mobility of pyroclastic flows and surges at the Soufriére Hills
623 Volcano, Montserrat. Geophys Res Lett 26:537–540. DOI 10.1029/1999GL900051

624 Calder ES, Sparks RSJ, Gardeweg MC (2000) Erosion, transport and segrega-
625 tion of pumice and lithic clasts in pyroclastic flows inferred from ignimbrite at
626 Láscar Volcano, Chile. J Volcanol Geotherm Res 104:201–235 DOI 10.1016/S0377-
627 0273(00)00207-9

628 Capasso L, Caramiello S, D'Anastasio R, Di Domenicantonio L, Di Fabrizio A, Di Nardo
629 F, La Verghetta M (2000) Paleobiologia della popolazione di Ercolano (79 d.C.).
630 Recenti Prog Med 91:288–296

631 Chadwick RA (1971) Paleomagnetic criteria for volcanic breccia emplacement. Geol Soc
632 Am Bull 82:2285–2294 DOI 10.1130/0016-7606(1971)82[2285:PCFVBE]2.0.CO;2

633 Cioni R, Gurioli L, Lanza R, Zanella E (2004) Temperatures of the AD 79 pyroclas-
634 tic density current deposits (Vesuvius, Italy). J Geophys Res 109:B02207. DOI
635 10.1029/2002JB002251

636 Clement BM, Conner CB, Graper G (1993) Paleomagnetic estimate of the emplacement
637 temperature of the long-runout Nevado De Colima Volcanic debris avalanche deposit,
638 Mexico. Earth Planet Sci Lett 120:499–510

639 Cole PD, Calder ES, Druitt TH, Hoblitt R, Robertson R, Sparks RSJ, Young SR
640 (1998) Pyroclastic flows generated by gravitational instability of the 1996–97 lava
641 dome of Soufriére Hills Volcano, Montserrat. Geophys Res Lett 25:3425–3428. DOI
642 10.1029/98gl01510

643 Crandell D (1971) Postglacial lahars from Mount Rainier Volcano, Washington. USGS
644 Professional Paper 677

645 Crandell DR, Mullineaux DR (1973) Pine Creek volcanic assemblage at Mount St.
646 Helens, Washington. USGS Bull 1383-A

647 Davila N, Capra L, Gavilanes-Ruiz JC, Varley N, Norini G, Vazquez AG (2007) Recent
648 lahars at Volcán de Colima (Mexico): drainage variation and spectral classification.
649 J Volcanol Geotherm Res 165:127–141 DOI 10.1016/j.jvolgeores.2007.05.016

650 De Gennaro M, Naimo D, Gialenella P, Incoronato A, Mastrolorenzo G (1996) Palaeo-
651 magnetic controls on the emplacement of the Neapolitan Yellow Tuff (Campi Flegrei,
652 Southern Italy). In: Morris A, Tarling DH (eds) Palaeomagnetism and tectonics of
653 the Mediterranean region. Geol Soc London Spec Pub 105:359–365

654 Denniss AM, Carlton RWT, Harris AJL, Rothery DA, Francis PW (1998) Satellite
655 observations of the April 1993 eruption of Láscar Volcano. Int J Rem Sens 19:801–
656 821 DOI 10.1080/014311698215739

657 Déruelle B, Medina ET, Figueroa OA, Maragano MC, Viramonté JG (1995) The recent

658 eruption of Láscar volcano (Atacama-Chile, April 1993): petrological and volcanolog-
659 ical relationships. C R Acad Sci Paris 321:377–384

660 Déruelle B, Figueroa OA, Medina ET, Viramonté JG, Maragano MC (1996) Petrology
661 of pumices of April 1993 eruption of Láscar (Atacama, Chile). Terra Nova 8:191–199
662 DOI 10.1111/j.1365-3121.1996.tb00744.x

663 Di Vito MA, Zanella E, Gurioli L, Lanza R, Sulpizio R, Bishop J, Tema E, Boenzi
664 G, Laforgia E (2009) The Afragola settlement near Vesuvius, italy: the destruction
665 and abandonment of a Bronze Age village revealed by archaeology, volcanology and
666 rock-magnetism. Earth Planet Sci Lett 277:408–421 DOI 10.1016/j.epsl.2008.11.006

667 Downey WS, Tarling DH (1991) Reworking characteristics of Quaternary pyroclastics,
668 Thera (Greece), determined using magnetic properties. J Volcanol Geotherm Res
669 46:143–155 DOI 10.1016/0377-0273(91)90080-J

670 Druitt TH, Calder ES, Cole PD, Hoblitt RP, Loughlin SC, Norton GE, Ritchie LJ,
671 Sparks RSJ, Voight B (2002) Small-volume, highly mobile pyroclastic flows formed
672 by rapid sedimentation from pyroclastic surges at Soufriere Hills Volcano, Montser-
673 rat; an important volcanic hazard. In: Druitt DH, Kokelaar B (eds) The eruption
674 of Soufriére Hills Volcano, Montserrat, from 1995 to 1999. Mem Geol Soc London
675 21:263–279

676 Dunlop DJ (1971) Magnetic properties of fine-particle hematite. Ann Geophys 27:269–
677 293

678 Erwin PS (2001) Palaeomagnetic investigations of volcano instability. PhD thesis, Uni-
679 versity of Oxford, Oxford

680 Fabian, K (2003) Statistical theory of weak field thermoremanent magnetization in
681 multidomain particle ensembles. Geophys J Int 155:479–488 DOI 10.1046/j.1365-
682 246X.2003.02057.x

683 Fisher RA (1953) Dispersion on a sphere. Proc R Soc London A217:295–305 DOI
684 10.1098/rspa.1953.0064

685 Grubensky MJ, Smith GA, Geissman JW (1998) Field and paleomagnetic characteri-
686 zation of lithic and scoriaceous breccias at Pleistocene Broken Top volcano, Oregon
687 Cascades. J Volcanol Geotherm Res 83:93–114 DOI 10.1016/S0377-0273(98)00006-7

688 Hoblitt RP, Kellogg KS (1979) Emplacement temperatures of unsorted and unstratified
689 deposits of volcanic rock debris as determined by paleomagnetic techniques. Geol Soc
690 Am Bull 90:633–642

691 Hoblitt RP, Reynolds RL, Larson EE (1985) Suitability of nonwelded pyroclastic-flow
692 deposits for studies of magnetic secular variation: a test based on deposits emplaced
693 at Mount St. Helens, Washington, in 1980. Geology 13:242–245 DOI 10.1130/0091-
694 7613(1985)13<242:SONPDF>2.0.CO;2

695 Kent DV, Ninkovitch D, Pescatore T, Sparks RSJ (1981) Palaeomagnetic determination
696 of emplacement temperature of the Vesuvius AD 79 pyroclastic deposits. Nature
697 290:393–396 DOI 10.1038/290393a0

698 Kirschvink JL (1980) The least-squares line and plane and the analysis of palaeomag-
699 netic data. Geophys J R Astr Soc 62:699–718

700 Leonhardt R (2006) Analyzing rock magnetic measurements: the RockMagAnalyzer
701 1.0 software. Comput Geosci 32:1420–1431

702 Levi, S (1977) Effect of magnetite particle-size on paleointensity determinations
703 of geomagnetic-field. Phys Earth Planet Inter 13:245–259 DOI 10.1016/0031-
704 9201(77)90107-8

705 Mandeville C, Carey S, Sigurdsson H, King J (1994) Paleomagnetic evidence for high-
706 temperature emplacement of the 1883 subaqueous pyroclastic flows from Krakatau
707 Volcano, Indonesia. J Geophys Res 99:9487–9504. DOI 10.1029/94jb00239

Mastrolorenzo G, Petrone PP, Pagano M, Incoronato A, Baxter PJ, Canzanella A, Fattore L (2001) Herculaneum victims of Vesuvius in AD 79. Nature 410:769–770 DOI 10.1038/35071167

Maury R (1971) Application de la spectrometrie infra-rouge a l'etude des bois fossilises dans les formations volcaniques. Bull Soc Géol France 5:280

McClelland E, Druitt DH (1989) Palaeomagnetic estimates of emplacement temperatures of pyroclastic deposits on Santorini, Greece. Bull Volcanol 51:16–27 DOI 10.1007/BF01086758

McClelland E, Erwin PS (2003) Was a dacite dome implicated in the 9,500 BP collapse of Mt Ruapehu? A palaeomagnetic investigation. Bull Volcanol 65:294–305 DOI 10.1007/s00445-002-0261-y

McClelland E, Thomas R (1993) A palaeomagnetic study of Minoan age tephra from Thera. In: Hardy D (ed) Thera and the Aegean World III. Thera Foundation, London pp 2:129–138

McClelland E, Wilson CJN, Bardot L (2004) Palaeotemperature determinations for the 1.8-ka Taupo ignimbrite, New Zealand, and implications for the emplacement history of a high-velocity pyroclastic flow. Bull Volcanol 66:492–513 DOI 10.1007/s00445-003-0335-5

McFadden PL, McElhinny MW (1990) Classification of the reversal test in palaeomagnetism. Geophys J Int 103:725–729 DOI 10.1111/j.1365-246X.1990.tb05683.x

Moore JD, Geissman JW, Smith GA (1997) Paleomagnetic emplacement-temperature and thermal-profile estimates for nonwelded pyroclastic-flow deposits, Miocene Peralta Tuff, Jemez Mountains, New Mexico. EOS Trans AGU 78:178

Mullineaux DR, Crandell DR (1962) Recent lahars from Mount St. Helens, Washington. Geol Soc Am Bull 73:855–870

733 Néel L (1949) Théorie du traînage magnétique des ferromagnétiques en grains fins avec
734 applications aux terres cuites. Ann Geophys 5:99–136

735 Oppenheimer C, Glaze LS, Francis PW, Rothery DA, Carlton RWT (1993) Infrared
736 image analysis of volcanic thermal features: Láscar Volcano, Chile, 1984–1992. J
737 Geophys Res 98:4269–4286. DOI 10.1029/92jb02134

738 Pares JM, Marti J, Garces M (1993) Thermoremanence in red sandstone clasts and
739 emplacement temperature of a Quaternary pyroclastic deposit (Catalan Volcanic
740 Zone, NE Spain). Stud Geophys Geod 37:401–414

741 Petrovský E, Kapička A (2006) On determination of the Curie point from thermomag-
742 netic curves. J Geophys Res 111:B12S27. DOI 10.1029/2006JB004507

743 Porreca, M, Giordano, G, Mattei, M, Musacchio, P (2006) Evidence of two Holocene
744 phreatomagmatic eruptions at Stromboli volcano (Aeolian Islands) from paleomag-
745 netic data. Geophys Res Lett 33:L21316. DOI 10.1029/2006GL027575

746 Porreca M, Mattei M, Mac Niocaill C, Giordano G, McClelland E, Funiciello R (2007)
747 Paleomagnetic evidence for low-temperature emplacement of the phreatomagmatic
748 Peperino Albano ignimbrite (Colli Albani volcano, Central Italy). Bull Volcanol
749 70:877–893 DOI 10.1007/s00445-007-0176-8

750 Pullaiah G, Irving E, Buchan KL, Dunlop DJ (1975) Magnetization changes caused
751 by burial and uplift. Earth Planet Sci Lett 28:133–143 DOI 10.1016/0012-
752 821X(75)90221-6

753 Rayleigh L (1919) On a problem of vibrations, and of random flights in one, two and
754 three dimensions. Phil Mag 37:321–347

755 Saito T, Ishikawa N, Kamata H (2003) Identification of magnetic minerals carry-
756 ing NRM in pyroclastic-flow deposits. J Volcanol Geotherm Res 126:127–142 DOI
757 10.1016/S0377-0273(03)00132-X

758 Saucedo R, Macías JL, Bursik MI, Mora JC, Gavilanes JC, Cortes A (2002) Emplace-
759 ment of pyroclastic flows during the 1998–1999 eruption of Volcán de Colima, Mexico.
760 J Volcanol Geotherm Res 117:129–153 DOI 10.1016/S0377-0273(02)00241-X

761 Saucedo R, Macías JL, Bursik MI (2004) Pyroclastic flow deposits of the 1991 eruption
762 of Volcán de Colima, Mexico. Bull Volcanol 66:291–306 DOI 10.1007/s00445-003-
763 0311-0

764 Saucedo R, Macías JL, Sheridan MF, Bursik MI, Komorowski JC (2005) Modeling of
765 pyroclastic flows of Colima Volcano, Mexico: implications for hazard assessment. J
766 Volcanol Geotherm Res 139:103–115 DOI 10.1016/j.jvolgeores.2004.06.019

767 Sawada Y, Sampei Y, Hyodo M, Yagami T, Fukue M (2000) Estimation of emplacement
768 temperatures of pyroclastic flows using H/C ratios of carbonized wood. J Volcanol
769 Geotherm Res 104:1–20, DOI 10.1016/S0377-0273(00)00196-7

770 Shcherbakova VV, Shcherbakov VP, Heider F (2000) Properties of partial thermore-
771 manent magnetization in pseudosingle domain and multidomain magnetite grains. J
772 Geophys Res 105:767–781. DOI 10.1029/1999JB900235

773 Smith GA, Grubensky MJ, Geissman JW (1999) Nature and origin of cone-forming
774 volcanic breccias in the Te Herenga Formation, Ruapehu, New Zealand. Bull Volcanol
775 61:64–82 DOI 10.1007/s004450050263

776 Smithsonian Institution (1980) Mount St. Helens. Scientific Event Alert Network
777 (SEAN) Bulletin 5

778 Smithsonian Institution (1993) Láscar. Scientific Event Alert Network (SEAN) Bulletin
779 18

780 Sparks RSJ, Gardeweg MC, Calder ES, Matthews SJ (1997) Erosion by pyroclastic flows
781 on Láscar volcano Chile. Bull Volcanol 58:557–565 DOI 10.1007/s004450050162

Sulpizio R, Mele D, Dellino P, La Volpe L (2005) A complex, Subplinian-type eruption from low-viscosity, phonolitic to tephri-phonolitic magma: the AD 472 (Pollena) eruption of Somma-Vesuvius, Italy. Bull Volcanol 67:743–767 DOI 10.1007/s00445-005-0414-x

Sulpizio R, Mele D, Dellino P, La Volpe L (2007) Deposits and physical properties of pyroclastic density currents during complex Subplinian eruptions: the AD 472 (Pollena) eruption of Somma-Vesuvius, Italy. Sedimentology 54:607–635 DOI 10.1111/j.1365-3091.2006.00852.x

Sulpizio R, Zanella E, Macías JL (2008) Deposition temperature of some PDC deposits from the 1982 eruption of El Chichón volcano (Chiapas, Mexico) inferred from rock-magnetic data. J Volcanol Geotherm Res 175:494–500 DOI 10.1016/j.jvolgeores.2008.02.024

Tamura Y, Koyama M, Fiske RS (1991) Paleomagnetic evidence for hot pyroclastic debris flow in the shallow submarine Shirahama Group (Upper Miocene-Pliocene) Japan. J Geophys Res 96:21779–21787. DOI 10.1029/91jb02258

Tanaka H, Hoshizumi H, Iwasaki Y, Shibuya H (2004) Applications of paleomagnetism in the volcanic field: a case study of the Unzen Volcano, Japan. Earth Planets Space 56:635–647

Tanguy J-C, Le Goff M, Principe C, Arrighi S, Chillemi V, Paiotti A, La Delfa S, Patanè G (2003) Archeomagnetic dating of Mediterranean volcanics of the last 2100 years: validity and limits. Earth Planet Sci Lett 211:111–124 DOI 10.1016/S0012-821X(03)00186-9

Tanguy J-C, Ribiere C, Scarth A, Tjetjep WS (1998) Victims from volcanic eruptions: a revised database. Bull Volcanol 60:137–144 DOI 10.1007/s004450050222

Tarling DH (1983) Palaeomagnetism: Principles and Applications in Geology, Geophysics and Archaeology. Chapman and Hall, London

Tsuboi S, Tsuya H (1930) On the temperature of the pumiceous ejecta of Komagatake, Hokkaidò, as inferred from their modes of oxidation. Bull Earthq Res Inst Univ Tokyo 8:271–273

Voight B, Davis MJ (2000) Emplacement temperatures of the November 22, 1994 nuée ardente deposits, Merapi Volcano, Java. J Volcanol Geotherm Res 100:371–377 DOI 10.1016/S0377-0273(00)00146-3

Witham CS (2005) Volcanic disasters and incidents: a new database. J Volcanol Geotherm Res 148:191–233 DOI 10.1016/j.jvolgeores.2005.04.017

Wooster MJ (2001) Long-term infrared surveillance of Láscar Volcano: contrasting activity cycles and cooling pyroclastics. Geophys Res Lett 28:847–850. DOI 10.1029/2000gl011904

Wooster MJ, Rothery DA (1997) Thermal monitoring of Láscar volcano, Chile, using infrared data from the along-track scanning radiometer: a 1992–1995 time series. Bull Volcanol 58:566–579 DOI 10.1007/s004450050163

Wooster MJ, Carlton RWT, Rothery DA, Sear CB (1998) Monitoring the development of active lava domes using data from the ERS-1 along track scanning radiometer. Adv Space Res 21:501–505 DOI 10.1016/S0273-1177(97)00887-9

Wright J (1978) Remanent magnetism of poorly sorted deposits from the Minoan eruption of Santorini. Bull Volcanol 41:131–135 DOI 10.1007/BF02597026

Xu WX, Peacor DR, VanderVoo R, Dollase W, Beaubouef R (1996) Modified lattice parameter Curie temperature diagrams for titanomagnetite/titanomaghemite within the quadrilateral Fe_3O_4–Fe_2TiO_4–Fe_2O_3–Fe_2TiO_5. Geophys Res Lett 23:2811–2814. DOI 10.1029/96GL01117

Yamazaki T, Kato I, Muroi I, Abe M (1973) Textural analysis and flow mechanism of the Donzurubo subaqueous pyroclastic flow deposits. Bull Volcanol 37:231–244 DOI 10.1007/BF02597132

834 Zanella E, De Astis G, Lanza R (2001) Palaeomagnetism of welded, pyroclastic-fall
835 scoriae at Vulcano, Aeolian Archipelago. J Volcanol Geotherm Res 107:71–86 DOI
836 10.1016/S0377-0273(00)00298-5

837 Zanella E, Gurioli L, Pareschi MT, Lanza R (2007) Influences of urban fabric on pyro-
838 clastic density currents at Pompeii (Italy): 2. temperature of the deposits and hazard
839 implications. J Geophys Res 112:B05214. DOI 10.1029/2006JB004775

840 Zanella E, Gurioli L, Lanza R, Sulpizio R, Bontempi M (2008) Deposition temperature
841 of the AD 472 Pollena pyroclastic density current deposits, Somma-Vesuvius, Italy.
842 Bull Volcanol 70:1237–1248 DOI 10.1007/s00445-008-0199-9

843 Zijderveld JDA (1967) A.C. demagnetization of rocks: Analysis of results. In: Collinson
844 DW, Creer KM, SK Runcorn SK (eds) Methods in Palaeomagnetism. Elsevier, New
845 York, pp 256–286

846 Zlotnicki J, Pozzi JP, Boudon G, Moreau MG (1984) A new method for the determi-
847 nation of the setting temperature of pyroclastic deposits (example of Guadeloupe
848 - French-West-Indies). J Volcanol Geotherm Res 21:297–312 DOI 10.1016/0377-
849 0273(84)90027-1

850 Zobin VM, Luhr JF, Taran YA, Bretón M, Cortés A, De La Cruz-Reyna S, Domínguez
851 T, Galindo I, Gavilanes JC, Muñíz JJ, Navarro C, Ramírez JJ, Reyes GA, Ursúa
852 M, Velasco J, Alatorre E, Santiago H (2002) Overview of the 1997–2000 activity of
853 Volcán de Colima, México. J Volcanol Geotherm Res 117:1–19 DOI 10.1016/S0377-
854 0273(02)00232-9

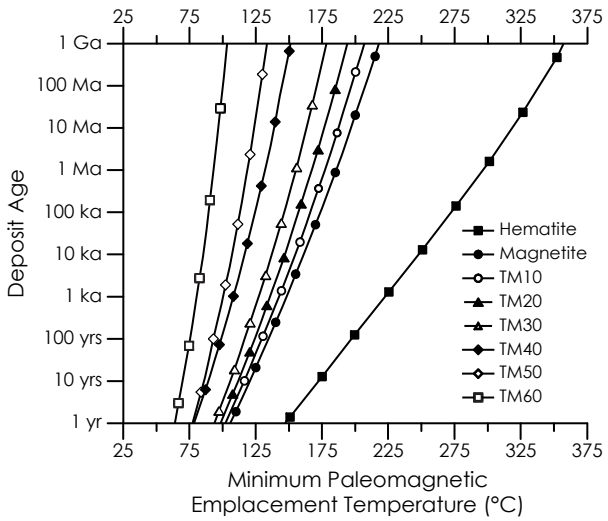

Figure 1: Deposit age plotted versus minimum paleomagnetic emplacement temperature as predicted by viscous magnetization theory for hematite, magnetite and part of the titanomagnetite series (TM10–TM60). The curves are based on theory and the magnetite data of Pullaiah et al. (1975) and hematite data from Dunlop (1971). The titanomagnetite series curves are calculated from the Curie temperature scaling relationship suggested by Pullaiah et al. (1975) using data from Xu et al. (1996).

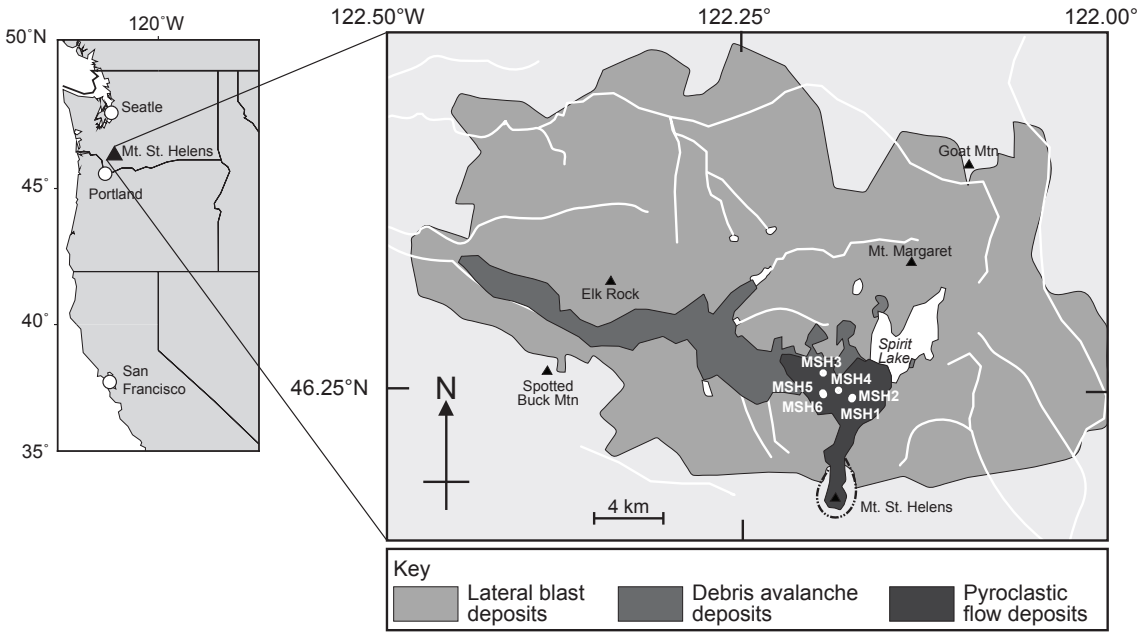

Figure 2: Location and map of the pyroclastic deposits from the 1980 eruption of Mt. St. Helens, with the sampled localities indicated (MSH1–6). Modified after Erwin (2001).

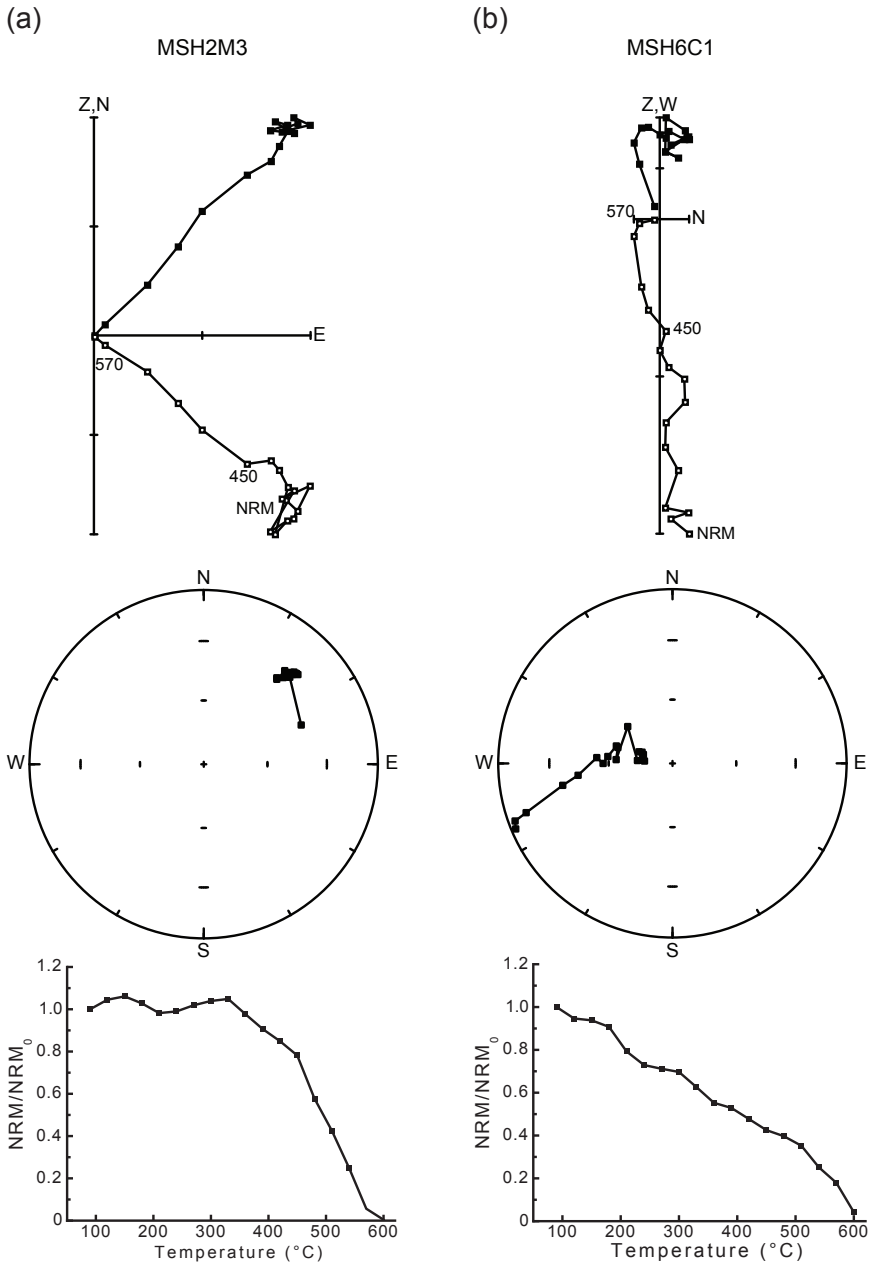

Figure 3: Typical stepwise thermal demagnetization behaviour for the Mt. St. Helens samples. (a) Sample MSH2M3 has a single component of magnetization. In this case the clast has been reworked, so the direction does not align with the 1980 geomagnetic field direction. (b) Sample MSH6C1 has two components of magnetization. The intersection of the two components is not clearly defined and covers a temperature range of 510–570°C. In the vector component diagrams (top), open symbols denote projections onto the vertical plane, while closed symbols denote projections onto the horizontal plane. In the equal area stereographic projections (middle), open symbols denote upper hemisphere projections, while closed symbols denote lower hemisphere projections.

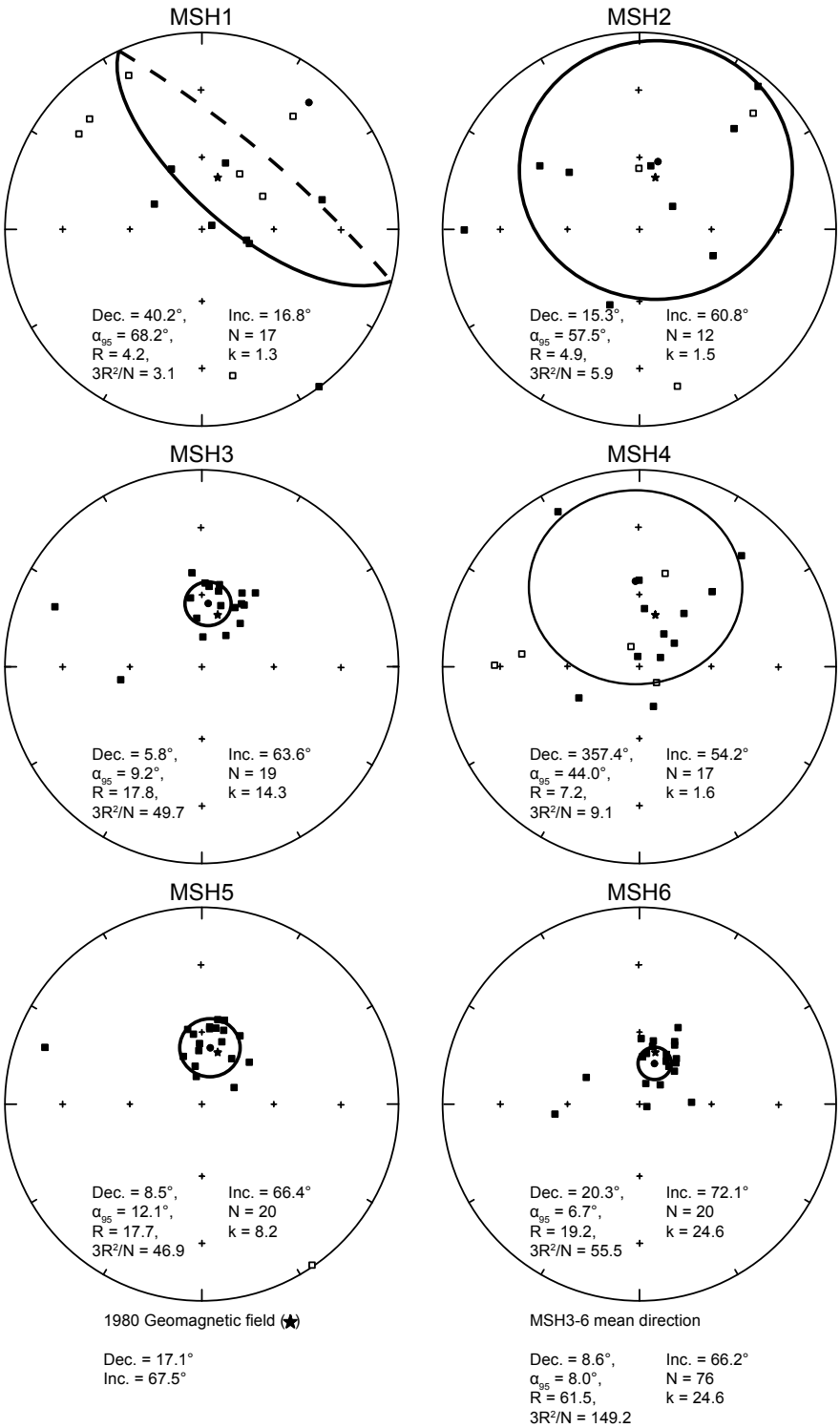

Figure 4: Equal area stereographic projections of paleomagnetic directions recorded at each sample site at Mt. St. Helens. The stars denote the 1980 geomagnetic field direction. The circles represent the mean directions and ellipses are the α_{95} cones of confidence about the mean. Open symbols denote upper hemisphere projections, while closed symbols denote lower hemisphere projections. Dec. = declination; Inc. = inclination; α_{95} = semi-angle of 95% confidence; N = number of samples; R = the length of the mean vector; k = the estimate of the precision parameter, from Fisher (1953); and $3R^2/N$ = the statistic for randomness from Rayleigh (1919).

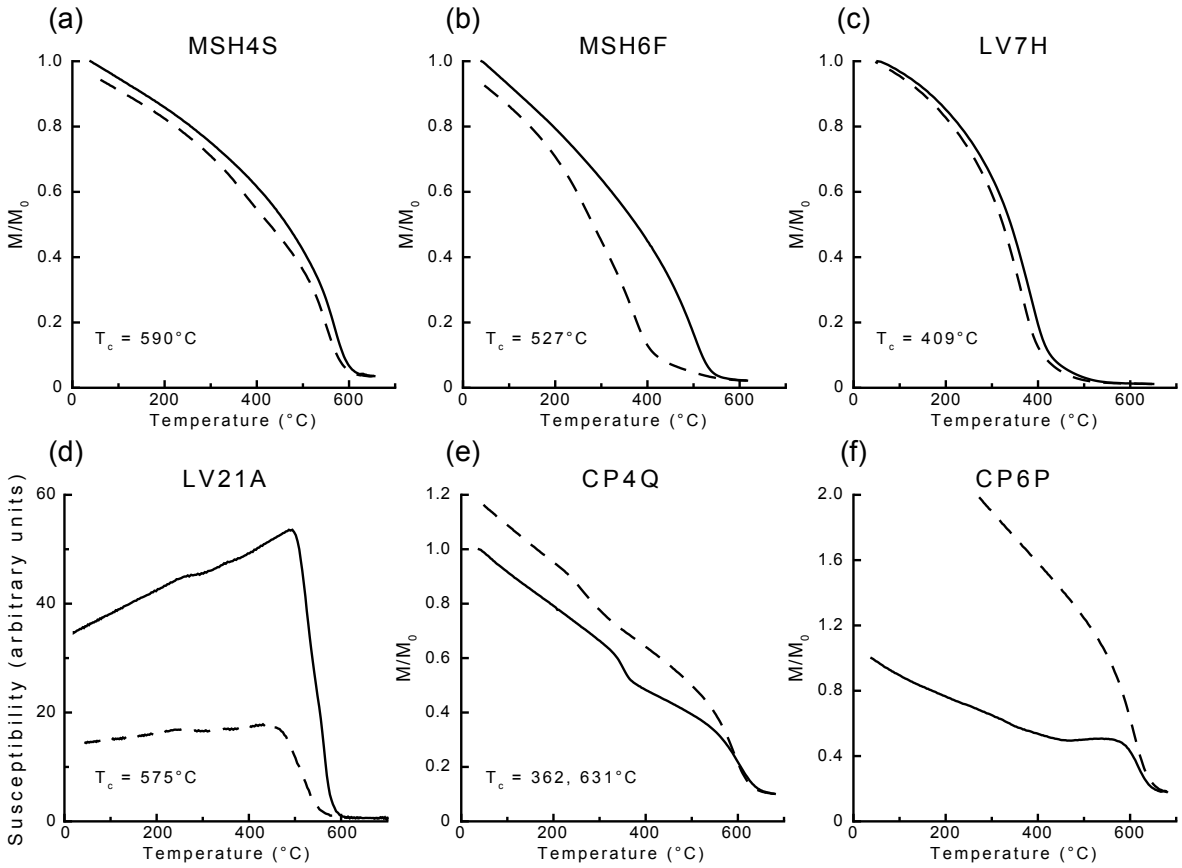

Figure 5: Typical thermomagnetic and susceptibility-temperature curves for samples from (a, b) Mt. St. Helens, (c, d) Láscar, and (e, f) Vesuvius. Solid (dashed) lines represent the heating (cooling) cycle. (a) Clast MSH4S, which has a Curie temperature of 590°C. (b) Clast MSH6F, $T_c = 527$°C. (c) Clast LV7H, $T_c = 409$°C. (d) Susceptibility-temperature curve for clast LV21A, $T_c = 575$°C. (e) Thermomagnetic curve for clast CP4Q, $T_c = 362, 631$°C. The coincidence of a Curie temperature with the emplacement temperature estimate may indicate that the remanence is of chemical and not thermal origin. (f) Thermomagnetic curve for clast CP6P, which is typical of maghemite inversion to hematite. The remanence carried by this clast is therefore likely to be a CRM.

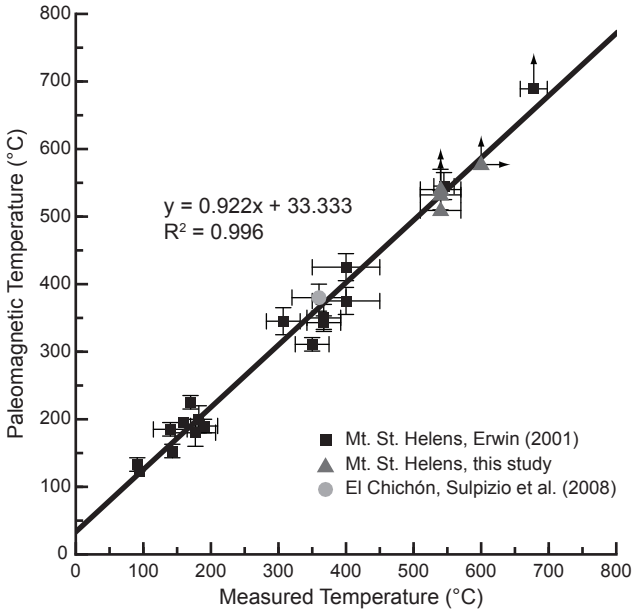

Figure 6: Paleomagnetic emplacement temperature versus directly measured emplacement temperature for the 1980 pyroclastic deposits at Mt. St. Helens, USA (Erwin, 2001, and this study), and El Chichón (Sulpizio et al., 2008). Both temperatures are strongly correlated, which indicates that the paleomagnetic approach is an accurate and viable method for determining the emplacement temperature of pyroclastic deposits. Small error bars have been removed for clarity; arrows indicate a minimum temperature estimate. Best-fit line calculated using major-axis linear regression.

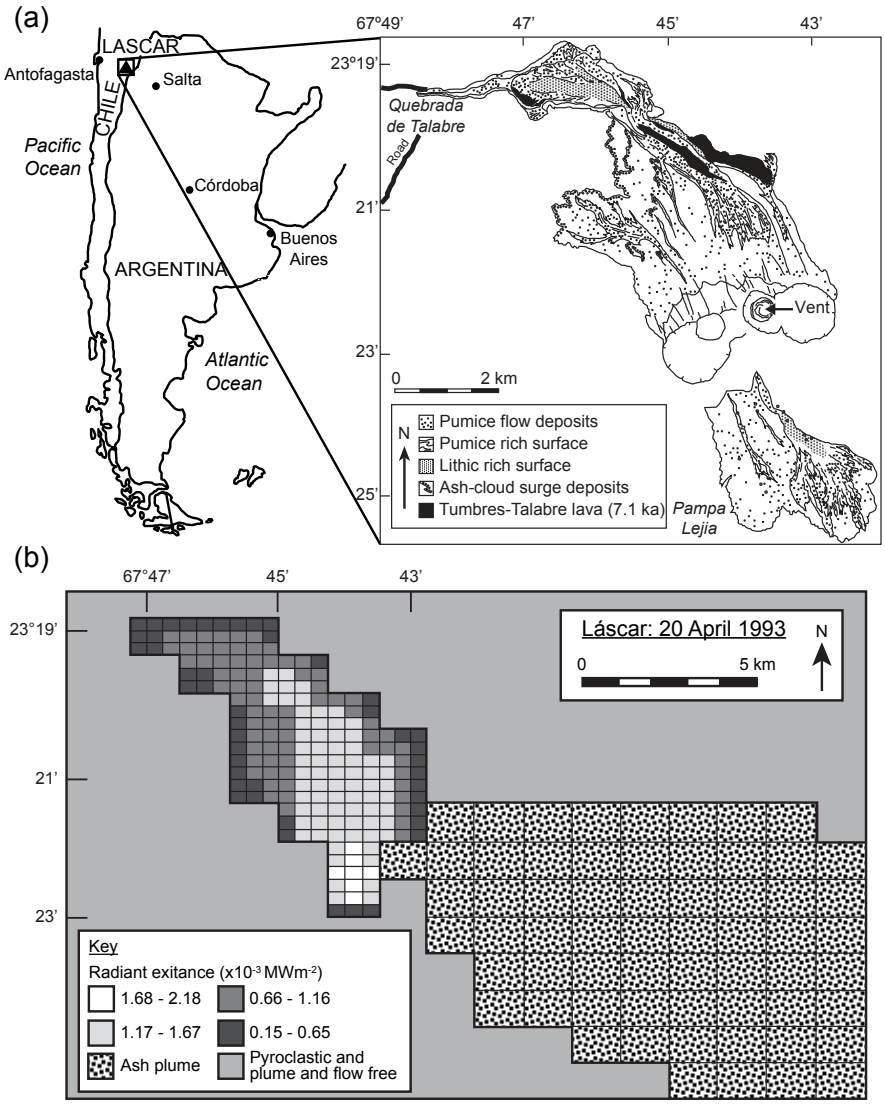

Figure 7: (a) Location map of Láscar volcano along with a simplified geological map of the deposits from the 18–20 April, 1993, pyroclastic density currents. The geological map has been modified after Calder et al. (2000). (b) Thermal radiance map of the 1993 Láscar pyroclastic deposits modified after Denniss et al. (1998). The shape of the northern thermal anomaly mimics the shape of the pyroclastic deposits shown in (a). The eruption cloud obscured the pyroclastic deposits on the SE slope of Láscar, so no thermal radiance data are available for these deposits.

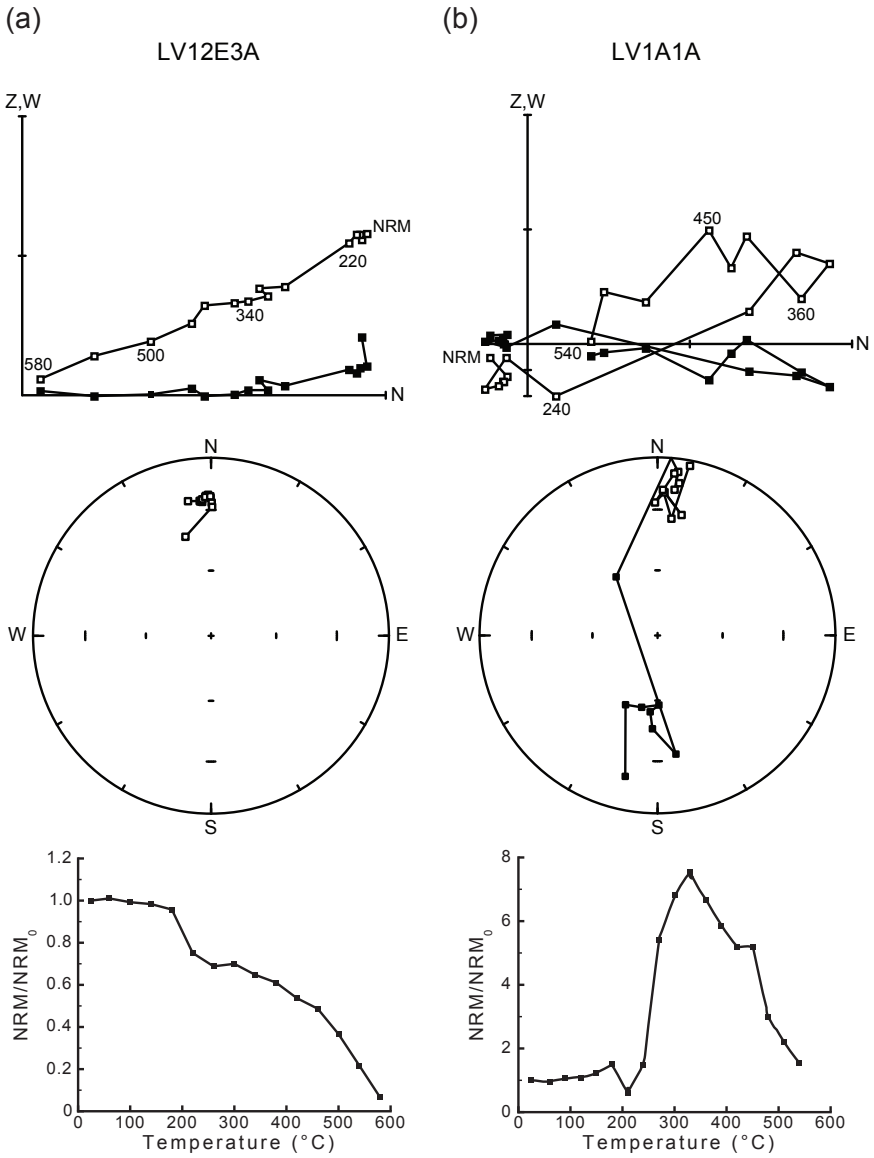

Figure 8: Typical stepwise thermal demagnetization behaviour for the Láscar samples. (a) Sample LV12E3A has a single component of magnetization that is aligned with the 1993 geomagnetic field direction. (b) Sample LV1A1A exhibits (noisy) self-reversing paleomagnetic behaviour, in which the high temperature component aligns with the expected geomagnetic direction and the low temperature component is anti-parallel to the expected direction. Symbols are the same as in Fig. 3.

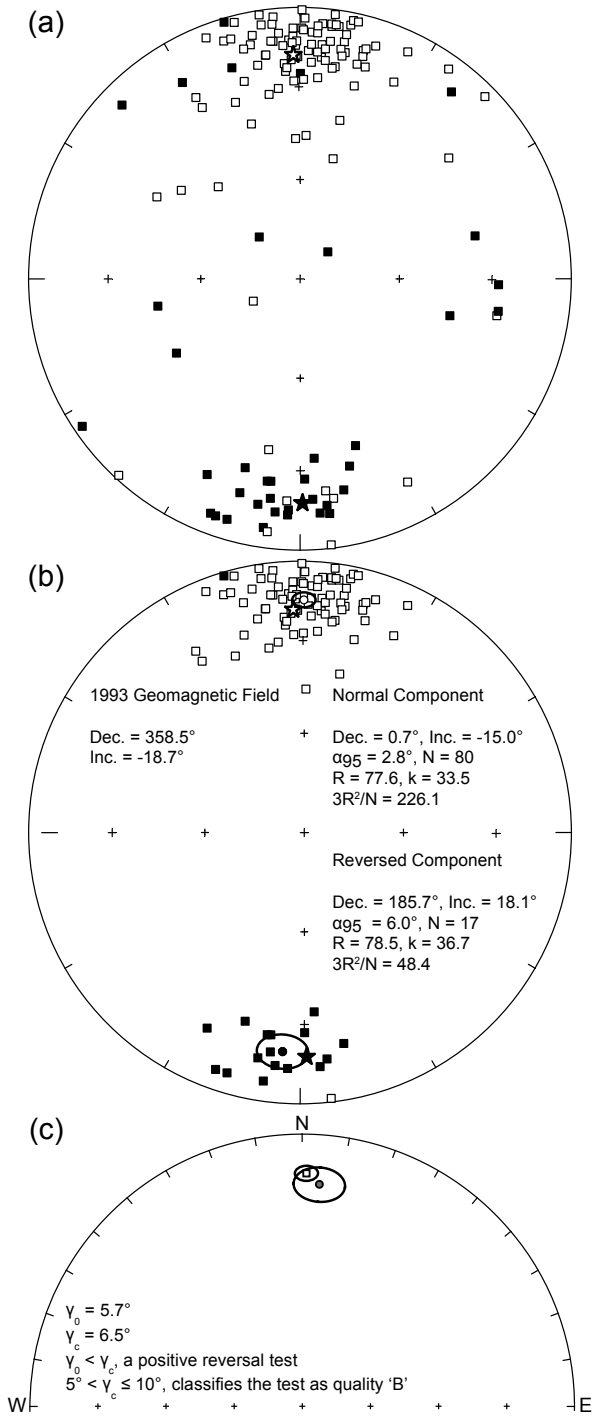

Figure 9: Equal area stereographic projections of the paleomagnetic directions recorded by the samples collected at Láscar. The open star represents the direction of the Earth's magnetic field during April 1993, and the filled star represents its antipode. (a) All of the recorded paleomagnetic directions. The distribution of directions is biased toward the direction of the 1993 geomagnetic field and its antipode (solid star). (b) The directions used for emplacement temperature estimation. The reversed polarity component represents data from 18 dacitic samples that exhibited self-reversing behaviour. Symbols are the same as in Fig. 4. (c) Reversal test for the mean paleomagnetic direction from the self-reversed samples compared to the mean direction for the normal polarity samples from Láscar. The open square represents the normally magnetized component and the grey circle represents the reversed polarity component with its declination rotated by 180°; the ellipses denote the respective α_{95} cones of 95% confidence. The overlapping confidence limits indicate that the directions are indistinguishable from a pair of antipodal directions. The reversal test of McFadden and McElhinny (1990) confirms this, and classifies the test as 'B' quality.

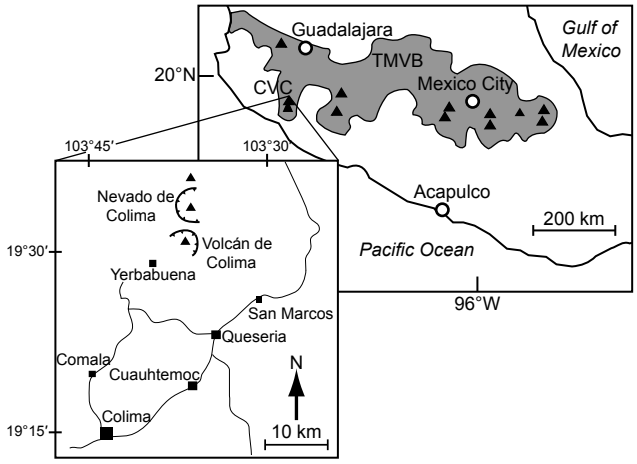

Figure 10: Map of Central Mexico with the location of the Colima Volcanic Complex (CVC) within the Trans-Mexican Volcanic Belt (TMVB). The inset contains an expanded view of the CVC; the lines represent the main roads. Modified after Saucedo et al. (2002).

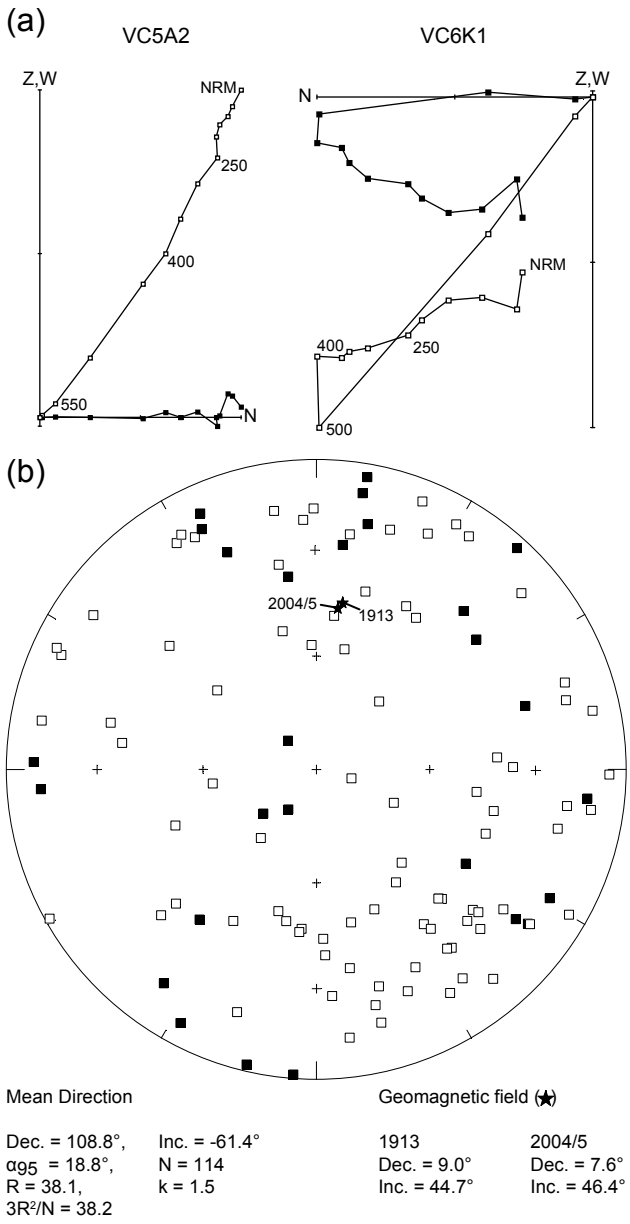

Figure 11: (a) Vector component diagrams for samples VC5A2 and VC6K1, which represent examples of single and multiple component remanent magnetizations, respectively. Symbols are the same as in Fig. 3. (b) Equal area stereographic projection of the low temperature paleomagnetic directions recorded by the studied samples from Colima. The two stars represent the expected geomagnetic field directions from 1913, 2004/2005, which are nearly indistinct. There is no statistically identifiable direction from the measured paleomagnetic data, although there is a general bias toward a southeastward and upward direction. Symbols are the same as in Fig. 4.

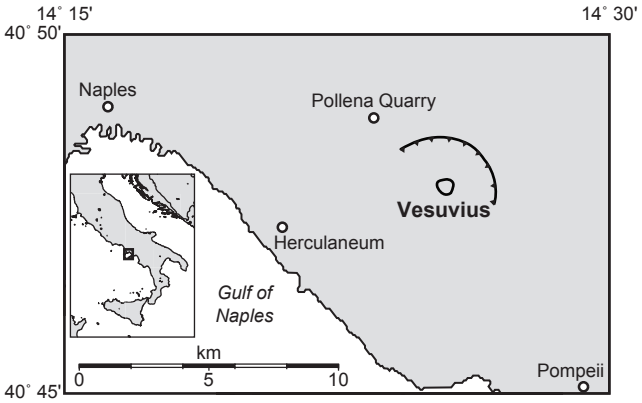

Figure 12: Sketch map of the Vesuvius area, central Italy. All samples were collected from Pollena quarry on the north-western flank of Vesuvius.

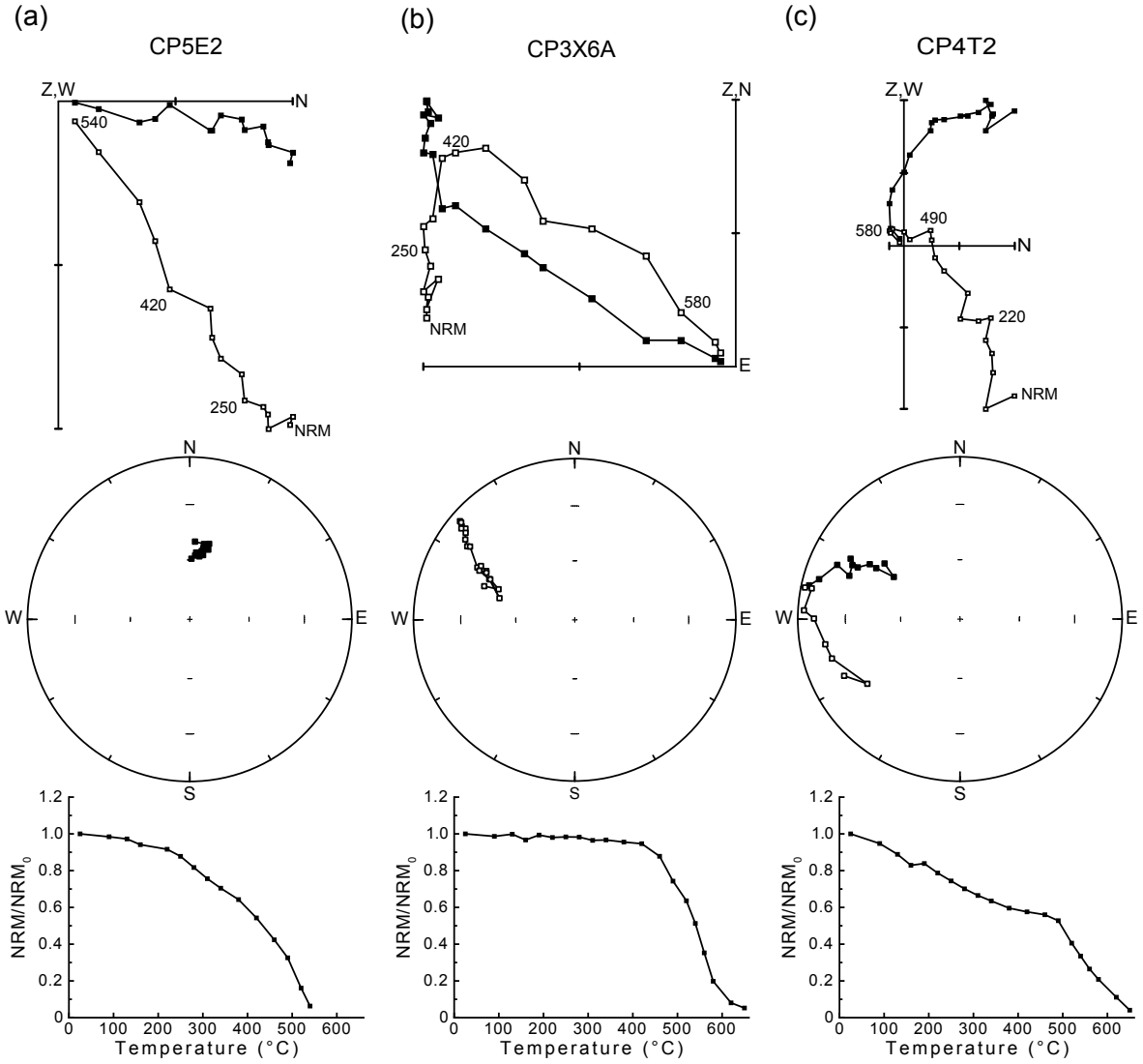

Figure 13: Typical stepwise thermal demagnetization behaviour for the Vesuvius samples. (a) Sample CP5E2 has a single component of magnetization that coincides with the mean paleomagnetic direction recorded at sites CP2-6. (b) Sample CP3X6A has two components of magnetization, with the low temperature direction aligning with the mean direction at site CP2–6. (c) Sample CP4T2 has three components of magnetization; the low temperature direction aligns with the expected mean direction, while neither higher temperature components have a preferred direction. Symbols are the same as in Fig. 3.

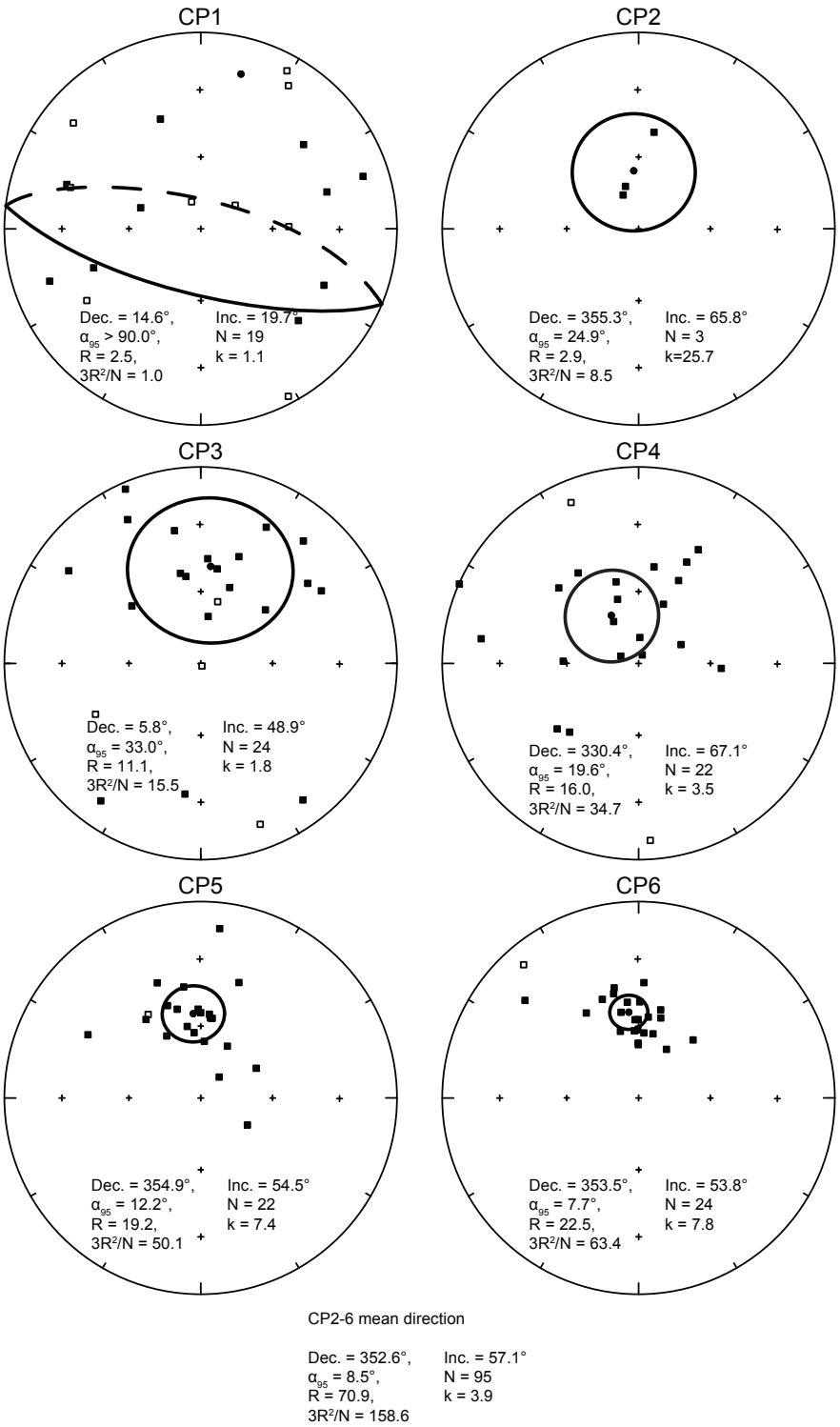

Figure 14: Equal area stereographic projections of paleomagnetic directions recorded at each sample site at Vesuvius. Symbols are the same as in Fig. 4.

Table 1: Previous studies using paleomagnetism to determine pyroclastic emplacement temperatures.

	Authors	**Location**	**Year**
1.	Aramaki and Akimoto	Asama, Bandai-san, Ko-Fuji	1957
2.	Mullineaux and Crandell	Mt. St. Helens	1962
3.	Chadwick	Gallatin Mountains	1971
4.	Crandell	Mt. St. Helens	1971
5.	Crandell and Mullineaux	Mt. St. Helens	1973
6.	Yamazaki et al.	Donzurubo	1973
7.	Wright	Santorini	1978
8.	Hoblitt and Kellogg	Mt. St. Helens	1979
9.	Kent et al.	Vesuvius	1981
10.	Zlotnicki et al.	Guadeloupe	1984
11.	McClelland and Druitt	Santorini	1989
12.	Downey and Tarling	Santorini	1991
13.	Tamura et al.	Shirahama Group	1991
14.	Clement et al.	Colima	1993
15.	McClelland and Thomas	Santorini	1993
16.	Pares et al.	Catalan Volc. Zone	1993
17.	Mandeville et al.	Krakatau	1994
18.	Bardot et al.	Santorini	1996
19.	De Gennaro et al.	Campi Flegrei	1996
20.	Moore et al.	Jemez Mountains	1997
21.	Grubensky et al.	Oregon Cascades	1998
22.	Smith et al.	Mt. Ruapehu	1999
23.	Bardot	Santorini	2000
24.	Bardot and McClelland	Santorini	2000
25.	Sawada et al.	Mt. Sambe	2000
26.	Mastrolorenzo et al.	Vesuvius	2001
27.	Zanella et al.	Vulcano	2001
28.	McClelland and Erwin	Mt. Ruapehu	2003
29.	Saito et al.	Yufu	2003
30.	Cioni et al.	Vesuvius	2004
31.	McClelland et al.	Taupo	2004
32.	Tanaka et al.	Unzen	2004
33.	Alva-Valdivia et al.	San Gaspar	2005
34.	Porreca et al.	Stromboli	2006
35.	Porreca et al.	Colli Albani	2007
36.	Zanella et al.	Vesuvius	2007
37.	Zanella et al.	Vesuvius	2008
38.	Sulpizio et al.	El Chicón	2008
39.	Di Vito et al.	Vesuvius	2009

Table 2: Emplacement temperature and paleomagnetic data from Mt. St. Helens, USA.

Sample	**Clast Type**	**T_e (°C)**	**Dec. (°)**	**Inc. (°)**	**N**	**MAD**	**T_c (°C)**
MSH3B7	Pumice	≥ 543	28.6	54.9	15	3.8	543
MSH3C4	Pumice	≥ 480	8.9	62.0	14	3.8	480
MSH3F3	Pumice	≥ 553	17.3	63.4	19	2.4	553
MSH3G6	Pumice	≥ 553	354.0	69.8	19	5.2	553
MSH3H4	Pumice	≥ 541	34.5	58.8	15	2.4	541
MSH3K1	Pumice	≥ 560	41.6	66.0	17	2.2	560
MSH3L2	Pumice	≥ 563	37.7	73.7	19	5.4	563
MSH3M7	Pumice	≥ 493	2.1	77.7	14	5.5	493
MSH3N1	Pumice	≥ 595	2.3	55.0	19	4.1	544, 595
MSH3O5	Pumice	≥ 470	32.2	59.0	17	3.4	470
MSH3P5	Pumice	≥ 527	12.1	54.9	15	3.0	527
MSH3Q1	Pumice	≥ 488	29.2	61.8	15	3.2	488
MSH3S1	Andesite	≥ 532	5.1	56.3	19	4.1	532
MSH3T1	Pumice	≥ 481	36.0	51.7	16	4.7	481
MSH3U1	Andesite	≥ 577	350.7	61.0	17	3.5	577
MSH3V3	Dacite	≥ 535	354.0	50.3	17	12.5	535
MSH3W5	Pumice	≥ 447	12.5	57.7	19	3.7	447
MSH4F7	Dacite	≥ 603	44.1	45.9	19	4.0	603
MSH4G6	Pumice	≥ 623	350.3	85.7	20	5.2	587, 623
MSH4M1	Dacite	≥ 592	5.0	65.8	17	2.9	592
MSH4Q1B	Dacite	≥ 598	66.2	80.5	20	5.2	598
MSH4S3	Dacite	≥ 590	36.7	73.1	19	3.2	590
MSH4T2	Pumice	≥ 626	56.0	72.6	19	4.2	593, 626
MSH4U2	Andesite	≥ 577	39.9	61.1	17	2.7	577
MSH4V2	Pumice	≥ 634	359.7	53.8	19	4.3	634
MSH5B3	Andesite	≥ 509	15.1	53.6	16	1.9	509
MSH5D4	Andesite	≥ 527	349.3	58.3	17	2.9	527
MSH5E4	Pumice	≥ 567	338.7	68.8	18	3.4	567
MSH5G2	Andesite	≥ 547	6.0	58.4	18	2.5	547
MSH5H1	Andesite	≥ 549	62.7	75.0	19	3.7	549
MSH5K1	Andesite	≥ 619	29.2	57.3	18	3.1	619
MSH5L1	Andesite	≥ 542	353.2	60.7	19	2.9	542
MSH5M4	Dacite	≥ 582	16.5	57.9	19	3.4	582
MSH5N4	Andesite	≥ 538	48.6	63.7	17	3.1	538
MSH5O2	Dacite	≥ 593	10.7	54.0	18	3.1	540, 593
MSH5P3	Vesicular Basalt	≥ 596	17.8	62.8	18	3.1	596
MSH5Q2	Dacite	≥ 563	356.8	67.8	19	6.4	563
MSH5R2	Andesite	≥ 516	10.5	57.7	19	2.2	516
MSH5S1	Andesite	≥ 535	33.3	67.4	19	6.5	535
MSH5T1	Andesite	≥ 559	357.8	64.8	18	6.7	559
MSH5U4	Andesite	≥ 617	5.8	57.6	16	2.5	553, 617
MSH5V3	Andesite	≥ 519	350.1	74.1	18	3.8	519

(continued on next page)

Table 2: *(continued)*

Sample	**Clast Type**	**T_e (°C)**	**Dec. (°)**	**Inc. (°)**	**N**	**MAD**	**T_c (°C)**
MSH5W1	Dacite	$\geq$ 607	348.8	78.4	19	3.7	607
MSH6B3A	Pumice	$\geq$ 533	296.7	65.3	18	3.7	533
MSH6C1	Reddened Dacite	510-570*	17.2	81.1	16	12.4	632
MSH6D3	Andesite	$\geq$ 557	108.0	86.8	17	3.9	557
MSH6E12	Pumice	$\geq$ 551	12.4	63.1	19	4.3	551
MSH6F3	Andesite	$\geq$ 527	1.5	62.7	16	4.2	527
MSH6G2	Andesite	$\geq$ 553	12.8	65.4	18	3.0	553
MSH6H4	Andesite	$\geq$ 634	37.8	70.1	18	4.1	589, 634
MSH6K2	Vesicular Basalt	$\geq$ 610	8.0	68.8	18	3.2	610
MSH6L1	Andesite	$\geq$ 602	46.7	70.1	19	2.9	602
MSH6M5	Pumice	$\geq$ 491	32.0	69.1	19	3.4	491
MSH6N2	Pumice	$\geq$ 570	28.5	66.6	19	2.7	570
MSH6O4	Andesite	$\geq$ 571	30.8	61.4	18	3.4	571
MSH6P4	Andesite	$\geq$ 560	47.1	78.3	18	3.3	560
MSH6Q1	Vesicular Basalt	$\geq$ 610	41.4	67.2	19	3.7	610
MSH6R6	Dacite	$\geq$ 592	3.6	70.3	19	3.4	592
MSH6S5	Andesite	$\geq$ 553	26.8	54.1	18	3.9	553
MSH6T2	Pumice	$\geq$ 564	29.4	60.1	19	3.8	564
MSH6U1	Andesite	$\geq$ 592	88.0	68.4	19	2.9	592
MSH6V5	Andesite	$\geq$ 585	39.1	65.7	18	3.1	585

Clast type identification based on microscopy, T_e = emplacement temperature, * denotes an estimate made from the intersection of two directional components; N = number of demagnetization steps used for the principal component analysis to determine the paleomagnetic direction for each sample (see Kirschvink 1980); MAD = maximum angular deviation (Kirschvink 1980); T_c = Curie temperature (determined from the heating cycle of a thermomagnetic experiment). Where two or more Curie temperatures are listed, multiple magnetic minerals are present in the sample.

Table 3: Emplacement temperature and paleomagnetic data from Láscar, Chile.

Sample	**Clast Type**	**T_e (°C)**	**Dec. (°)**	**Inc. (°)**	**N**	**MAD**	**T_c (°C)**
LV1A1A	Dacitic Pumice	$\geq$ 425	5.5	-19.1	10	10.6	425
LV1A2B	Dacitic Pumice	$\geq$ 425	5.0	-26.5	8	6.4	425
LV3B1	Reddened Andesite	$\geq$ 586	330.1	-24.0	16	6.7	586
LV3D2	Dacitic Pumice	$\geq$ 428	10.6	-12.2	12	13.9	428
LV4A1	Reddened Andesite	$\geq$ 641	15.7	-27.1	20	2.4	251, 469, 641
LV4C2	Andesite	$\geq$ 483	344.2	-25.4	20	5.3	483
LV5A1A	Dacitic Pumice	$\geq$ 420	357.3	-12.9	11	8.2	420
LV5B2B	Dacitic Pumice	$\geq$ 427	339.9	-31.4	11	10.3	427
LV5C3A	Dacitic Pumice	$\geq$ 447	25.4	-8.2	11	14.8	447
LV6A1	Andesite	$\geq$ 553	2.4	-46.1	20	6.8	553
LV6B1	Andesite	$\geq$ 439	8.3	-18.3	13	3.4	439
LV6C1	Andesite	$\geq$ 543	345.6	-2.8	16	4.9	543
LV6C5B	Andesite	$\geq$ 543	338.7	-5.3	14	2.7	543
LV6D1A	Andesite	$\geq$ 463	5.1	-6.3	18	4.8	463
LV6G5	Andesitic Pumice	$\geq$ 599	11.3	-5.2	20	4.5	599
LV6I2	Andesite	$\geq$ 420	7.2	-7.0	18	5.7	420
LV6I4A	Andesite	$\geq$ 420	2.8	-9.9	13	3.3	420
LV7B2	Andesite	$\geq$ 413	0.4	-8.4	12	4.4	413
LV7G2	Andesite	$\geq$ 543	353.5	-13.0	20	6.9	543
LV7H3	Andesite	$\geq$ 409	4.1	-10.1	20	5.4	409
LV8A5	Dacitic Pumice	$\geq$ 433	358.9	-15.0	10	7.7	433
LV9A1	Dacitic Pumice	$\geq$ 523	11.7	-3.2	19	5.5	523
LV9B1	Dacitic Pumice	$\geq$ 427	343.3	1.6	12	6.9	427
LV9D1A	Dacitic Pumice	$\geq$ 427	2.1	-17.0	11	9.7	427
LV9F3	Andesite	$\geq$ 568	5.4	-14.4	15	5.5	568
LV10B3	Dacitic Pumice	$\geq$ 428	8.8	-6.6	11	14.1	428
LV10C5	Dacitic Pumice	$\geq$ 456	10.8	-9.3	13	4.2	456
LV10D1	Dacitic Pumice	$\geq$ 517	348.8	-20.9	20	6.2	517
LV10D3B	Dacitic Pumice	$\geq$ 517	330.3	-28.2	15	3.8	517
LV11A1	Andesite	$\geq$ 405	15.5	-13.8	20	5.4	405
LV11B3	Dacitic Pumice	$\geq$ 481	1.0	-27.4	8	7.9	481
LV12A3	Reddened Andesite	$\geq$ 547	359.4	-19.3	19	4.2	547
LV12C1A	Dacitic Pumice	$\geq$ 432	4.4	-17.3	10	11.3	432
LV12D3	Dacite	$\geq$ 457	11.3	-16.1	20	3.6	457
LV12E1A	Reddened Andesite	$\geq$ 587	8.7	-22.6	20	3.8	587
LV12E3A	Reddened Andesite	$\geq$ 587	356.0	-24.4	15	2.8	587
LV13A4	Dacitic Pumice	$\geq$ 427	346.2	-13.9	11	3.6	427
LV14C1A	Dacitic Pumice	$\geq$ 436	10.1	-15.2	19	10.9	436
LV15B3	Dacite	$\geq$ 527	10.7	-17.6	20	4.8	407, 527
LV16A1A	Dacite	$\geq$ 513	354.1	-3.4	19	14.0	513
LV16A3B	Dacite	$\geq$ 513	355.0	-10.1	14	6.6	513
LV16B1A	Andesite	$\geq$ 414	7.1	-6.0	17	7.0	414

(continued on next page)

Table 3: *(continued)*

Sample	**Clast Type**	**T_e (°C)**	**Dec. (°)**	**Inc. (°)**	**N**	**MAD**	**T_c (°C)**
LV16C2	Dacitic Pumice	$\geq$ 417	6.6	-20.1	11	10.0	417
LV17A2	Andesite	$\geq$ 426	355.8	-21.6	20	5.8	426
LV18B2	Andesite	$\geq$ 427	8.1	-6.1	20	7.2	427
LV19B2	Dacite	$\geq$ 534	4.1	-7.3	19	3.2	534
LV19C2	Andesite	$\geq$ 518	353.0	-12.8	19	3.8	468, 518
LV19D2	Andesite	$\geq$ 510	348.9	-9.5	18	6.1	510
LV19E2	Dacite	$\geq$ 523	351.2	-1.8	20	8.1	523
LV19F1	Dacite	$\geq$ 523	358.3	-11.6	20	4.2	463, 523
LV19G1A	Dacite	$\geq$ 533	6.3	-15.9	20	6.3	533
LV20B2	Dacite	$\geq$ 527	12.8	-3.3	20	5.7	527
LV20C1	Dacite	$\geq$ 444	359.2	-13.4	20	3.4	444
LV21A1	Andesite	$\geq$ 575	358.4	-8.4	19	3.8	575
LV21B3	Dacite	$\geq$ 397	7.3	-12.8	18	4.2	397
LV21C2	Andesite	$\geq$ 573	3.0	-21.2	19	3.8	573
LV22A1B	Dacitic Pumice	$\geq$ 444	353.7	-6.3	11	15.0	444
LV22C2A	Dacitic Pumice	$\geq$ 440	18.0	-10.8	9	8.9	440
LV22C2B	Dacitic Pumice	$\geq$ 440	15.8	-16.0	9	8.0	440
LV22D2	Andesite	$\geq$ 573	353.5	-30.1	17	7.9	573
LV23A1	Andesite	$\geq$ 417	2.8	-14.6	18	8.3	417
LV23D2	Dacitic Pumice	$\geq$ 417	350.5	-31.7	9	8.0	417
LV24A1	Dacitic Pumice	$\geq$ 447	351.2	-17.8	8	8.5	447
LV24B2	Dacitic Pumice	$\geq$ 483	351.3	-17.7	9	11.2	413, 483
LV25C2B	Dacite	$\geq$ 463	17.1	-19.5	20	4.1	463
LV26A1	Dacitic Pumice	$\geq$ 413	16.0	-12.9	8	8.2	413
LV26B	Dacitic Pumice	$\geq$ 417	25.5	-20.8	15	3.8	417
LV26B2	Dacitic Pumice	$\geq$ 417	356.4	-23.1	10	7.6	417
LV26D1	Andesite	$\geq$ 401	342.2	-8.8	14	6.5	401
LV27B1	Dacite	$\geq$ 413	0.8	-9.1	14	7.9	413
LV28C2	Dacitic Pumice	$\geq$ 443	358.2	-27.9	8	4.2	443
LV28E1	Andesite	$\geq$ 477	357.7	-20.3	16	6.6	477
LV29B3B	Andesite	$\geq$ 434	1.1	-4.4	20	12.6	434
LV29C2	Dacitic Pumice	$\geq$ 443	343.9	-8.9	11	13.4	443
LV29E1A	Dacitic Pumice	$\geq$ 452	355.8	-14.9	11	9.0	402, 452
LV30A4	Andesitic Pumice	$\geq$ 543	7.6	-2.0	20	9.9	543
LV30B1	Dacite	$\geq$ 483	0.4	-1.0	20	5.2	483
LV30C4	Dacitic Pumice	$\geq$ 425	358.1	-14.0	12	6.2	425
LV30D2	Andesite	$\geq$ 423	14.1	-39.6	20	6.5	423
LV31C5	Dacitic Pumice	$\geq$ 433	351.3	-6.0	10	7.5	433

Symbols are the same as in Table 2.

Table 4: Emplacement temperature and paleomagnetic data from Colima, Mexico.

Sample	**Clast Type**	**Dec. (°)**	**Inc. (°)**	**N**	**MAD**
VC1B	Dacite	145.2	-39.1	17	1.7
VC1D2	Andesite	91.0	-6.1	3	10.0
VC1E3	Olivine Andesite	98.4	-11.4	13	5.8
VC1E6	Olivine Andesite	98.3	-19.4	13	5.2
VC1F1	Andesite	136.5	-42.1	6	14.7
VC1H1	Olivine Andesite	310.1	-38.1	17	6.9
VC1K2	Andesite	144.3	-36.8	8	8.2
VC1L	Olivine Andesite	42.2	4.1	4	2.6
VC2B1	Dacite	282.8	-32.5	7	10.6
VC2B2	Dacite	240.8	-1.6	10	10.0
VC2E1	Olivine Andesite	142.8	-28.6	17	5.2
VC2E2	Olivine Andesite	153.4	-29.4	13	2.5
VC2G1	Andesite	126.1	16.7	17	4.6
VC2H	Andesite	144.8	-53.3	6	8.6
VC2K	Andesite	126.8	-25.6	10	6.0
VC2L1	Reddened Andesite	135.9	-41.4	6	14.2
VC3A1	Andesite	9.9	4.8	13	4.3
VC3C	Andesite	9.5	10.6	17	5.3
VC3D1	Reddened Dacite	315.5	79.4	13	9.7
VC3E2	Andesite	33.2	-11.1	17	3.9
VC3F1	Reddened Dacite	28.8	-39.7	13	5.0
VC3H2	Andesite	308.6	-56.4	3	7.5
VC3K4B	Dacite	78.0	-9.8	7	5.5
VC3K5A	Dacite	74.5	-17.6	7	5.1
VC3L3	Olivine Andesite	86.2	-41.2	4	13.3
VC4B3A	Andesite	195.0	-50.9	8	11.2
VC4C	Andesite	191.2	-48.7	8	3.4
VC4E	Andesite	176.0	-27.6	14	8.3
VC4G	Olivine Andesite	134.2	-27.1	11	7.1
VC4H1	Andesite	193.3	2.5	13	3.9
VC4K3	Andesite	170.4	-35.3	10	5.5
VC4L	Andesite	42.7	-65.6	18	3.7
VC5A2	Olivine Andesite	357.8	-57.0	13	2.5
VC5A4	Olivine Andesite	13.2	-57.3	13	3.8
VC5B1	Dacite	346.3	-52.1	17	1.2
VC5D3	Olivine Andesite	89.3	-36.7	13	4.7
VC5D6	Olivine Andesite	103.2	-40.9	13	4.8
VC5E1B	Reddened Dacite	185.3	-47.2	11	3.6
VC5E3	Reddened Dacite	186.0	-46.2	18	5.4
VC5E4	Reddened Dacite	177.3	-39.8	13	6.7
VC5F1	Reddened Dacite	125.9	-16.0	17	5.3
VC5F2	Reddened Dacite	122.2	42.5	13	5.0

(continued on next page)

Table 4: *(continued)*

Sample	**Clast Type**	**Dec. (°)**	**Inc. (°)**	**N**	**MAD**
VC5F2	Reddened Dacite	122.2	42.5	13	5.0
VC5H	Reddened Dacite	29.7	-9.9	17	7.7
VC5K2	Andesite	294.2	-10.8	9	7.4
VC5L	Andesite	328.3	-15.3	17	3.8
VC6A1	Reddened Dacite	15.4	-40.2	11	8.8
VC6B	Andesite	350.7	-16.6	17	5.0
VC6C	Andesite	6.7	27.9	18	8.7
VC6D1	Dacite	33.3	-41.1	9	8.3
VC6E1	Andesite	208.2	8.0	13	4.8
VC6F	Andesite	330.1	-13.7	17	3.7
VC6H	Dacite	6.6	-48.7	9	9.1
VC6K1	Andesite	17.1	-20.2	10	12.0
VC7A2	Andesite	11.8	20.3	13	8.7
VC7A3	Andesite	337.7	25.3	13	8.2
VC7C1	Andesite	119.9	-6.7	13	4.4
VC7D2B	Andesite	21.6	-7.8	13	3.5
VC7D3B	Andesite	25.3	-17.0	13	3.9
VC7E2	Olivine Andesite	359.4	-16.9	13	4.9
VC7F	Olivine Andesite	357.0	-20.5	13	6.5
VC7G	Dacite	49.3	-13.8	17	4.7
VC7H	Andesite	70.7	-16.2	3	7.2
VC7K	Andesite	8.1	-24.4	17	6.1
VC8A2	Andesite	226.8	-31.9	18	6.4
VC8B2	Dacite	304.7	-13.6	8	12.1
VC8C2	Andesite	335.6	10.2	9	14.1
VC8D2	Andesite	271.5	9.7	13	5.3
VC8D3	Andesite	265.9	11.9	18	5.1
VC8G2	Dacite	349.6	-33.3	8	10.0
VC8L	Andesite	280.1	-11.0	9	10.4
VC8M	Andesite	332.4	-16.6	9	10.8
VC9D2A	Olivine Andesite	103.8	-20.9	8	13.6
VC9F2	Reddened Andesite	215.0	77.2	13	5.9
VC9F3	Reddened Andesite	230.2	71.9	18	2.3
VC9K	Andesite	172.9	-13.9	17	3.2
VC9L	Olivine Andesite	198.1	-18.8	17	2.3
VC9M2A	Andesite	149.1	-17.1	13	4.5
VC9M4	Andesite	118.9	15.1	13	8.1
VC10A1	Dacite	219.0	-66.8	7	8.2
VC10B1	Reddened Andesite	50.9	33.9	13	6.6
VC10C	Andesite	277.8	-36.9	9	11.2
VC10D	Andesite	295.1	-8.3	12	11.2
VC10E1	Andesite	98.0	-46.7	13	5.8
VC10E2A	Andesite	113.3	-67.8	13	5.0

(continued on next page)

Table 4: *(continued)*

Sample	**Clast Type**	**Dec. (°)**	**Inc. (°)**	**N**	**MAD**
VC10F1	Andesite	334.5	15.2	13	3.8
VC10H	Olivine Andesite	184.3	1.5	18	3.5
VC10L2	Andesite	217.9	38.6	13	6.5
VC10L3	Andesite	157.6	-23.7	13	7.6
VC11A1	Andesite	262.3	-62.4	13	6.8
VC11F1	Reddened Andesite	73.1	30.2	13	1.8
VC11G1	Olivine Andesite	104.2	-80.5	8	14.1
VC11H1	Olivine Andesite	167.2	-48.1	17	4.5
VC11K1	Andesite	136.6	-42.2	13	3.6
VC11K4	Andesite	137.5	-56.5	13	2.9
VC11L2	Andesite	110.8	-41.2	11	12.7
VC12B1	Andesite	143.9	-29.2	5	5.5
VC12D1	Andesite	131.9	-32.7	7	9.5
VC12D4A	Andesite	131.4	-31.0	7	8.5
VC12E1	Andesite	163.9	-28.0	8	3.8
VC12G1	Olivine Andesite	157.5	-49.6	9	13.4
VC12H2	Olivine Andesite	96.1	13.1	15	7.6
VC12M1	Andesite	177.7	-44.5	13	4.5
VC12N1B	Andesite	226.3	-37.4	15	6.4
VC12N2A	Andesite	248.3	-49.5	15	4.6
VC12O2	Reddened Andesite	126.9	20.7	16	3.1
VC13B1A	Dacite	165.6	-16.8	14	2.6
VC13C1A	Olivine Andesite	139.8	-12.6	14	4.6
VC13D1	Reddened Dacite	351.7	37.2	15	4.0
VC13G2A	Olivine Andesite	135.1	-31.6	8	12.9
VC13L1	Olivine Andesite	208.7	-43.6	15	6.5
VC13M1A	Andesite	145.0	-18.9	13	4.5
VC13O2	Andesite	215.5	16.4	15	9.1
VC13P1	Reddened Andesite	42.9	30.9	12	11.0
VC13Q1A	Andesite	165.9	-22.7	6	5.1

Symbols are the same as in Table 2. Clast type identification based on hand specimen examination.

Table 5: Emplacement temperature and paleomagnetic data from Vesuvius, Italy.

Sample	**Clast Type**	**T_e (°C)**	**Dec. (°)**	**Inc. (°)**	**N**	**MAD**	**T_c (°C)**
CP2A3	Andesite	$\geq$ 573	335.4	74.6	12	3.1	573
CP2B1	Andesite	$\geq$ 580	342.9	71.6	9	3.2	580
CP2C3	Leucite Tephrite	$\geq$ 568	9.1	48.8	12	1.9	568
CP3A1B	Leucite Tephrite	310–380*	20.9	56.0	6	9.3	602
CP3B6	Leucite Tephrite	420*	3.8	45.6	7	13.4	607
CP3E2	Leucite Tephrite	380–420*	9.8	49.6	6	9.5	559
CP3O1	Andesite	$\geq$ 579	19.7	41.8	14	3.5	483, 579
CP3Q4B	Leucite Tephrite	$\geq$ 548	309.8	52.3	12	8.1	548
CP3S2	Leucite Tephrite	310–340*	347.3	51.2	6	12.1	547
CP3V12A	Leucite Tephrite	380*	348.8	31.7	8	10.9	537, 577
CP3X6A	Leucite Tephrite	420–460*	350.3	53.0	9	7.5	606
CP3Y2B	Leucite Tephrite	460*	9.0	70.3	9	13.1	611
CP4A2	Leucite Tephrite	380–420*	291.9	82.1	8	11.7	594
CP4B2B	Leucite Tephrite	420–460*	25.8	51.3	10	14.3	603
CP4E4	Leucite Tephrite	$\geq$ 589	329.1	69.8	14	4.0	589
CP4F2	Leucite Tephrite	490–520*	23.4	86.2	12	11.6	612
CP4H4B	Leucite Tephrite	340–380*	9.1	48.8	8	14.9	611
CP4I8A	Leucite Tephrite	280–340*	3.0	79.3	8	14.2	571
CP4J4B	Porphyritic Leucite Tephrite	$\geq$ 599	344.6	54.6	16	4.3	599
CP4P1B	Porphyritic Leucite Tephrite	$\geq$ 610	313.4	43.4	16	4.7	610
CP4T2	Porphyritic Leucite Tephrite	460–490*	341.8	61.9	10	9.8	628
CP4X3	Andesite	380–460*	326.2	43.9	8	12.7	553
CP4Y6	Porphyritic Leucite Tephrite	380–420*	25.4	42.4	8	12.2	553, 603
CP5A2A	Leucite Tephrite	$\geq$ 568	345.1	51.4	14	3.9	568
CP5C4B	Leucite Tephrite	$\geq$ 543	358.3	52.7	13	3.5	543
CP5E2	Andesite	$\geq$ 557	8.2	56.3	12	2.3	557
CP5F2	Leucite Tephrite	$\geq$ 580	340.2	48.6	11	2.8	580
CP5H1	Andesite	$\geq$ 555	339.3	37.4	15	5.1	555
CP5J2	Leucite Tephrite	$\geq$ 572	5.9	54.7	11	4.9	572
CP5K2B	Leucite Tephrite	$\geq$ 572	351.3	42.3	10	2.3	572
CP5L4	Leucite Tephrite	$\geq$ 572	18.3	38.1	15	3.3	572
CP5N1A	Leucite Tephrite	$\geq$ 569	325.1	49.7	15	5.1	569
CP5P2	Leucite Tephrite	$\geq$ 548	6.8	56.3	11	3.3	548
CP5Q1	Leucite Tephrite	$\geq$ 589	331.2	60.5	15	4.7	589
CP5S3	Leucite Tephrite	520*	356.1	60.8	14	4.0	559
CP5U1B	Leucite Tephrite	$\geq$ 560	27.2	65.8	12	2.7	560
CP5V1	Porphyritic Leucite Tephrite	$\geq$ 563	41.5	78.5	15	4.0	563
CP5X5	Leucite Tephrite	520*	337.3	73.5	15	5.8	577
CP5Y2	Leucite Tephrite	520*	1.2	51.5	13	3.8	568
CP5Z1	Leucite Tephrite	$\geq$ 562	349.3	59.6	12	2.5	562
CP6A3	Syenite	$\geq$ 649	6.8	55.9	15	3.1	649

(continued on next page)

Table 5: *(continued)*

Sample	**Clast Type**	**T_e (°C)**	**Dec. (°)**	**Inc. (°)**	**N**	**MAD**	**T_c (°C)**
CP6B4	Leucite Tephrite	≥ 572	14.1	51.8	11	3.8	572
CP6C2	Leucite Tephrite	≥ 573	357.4	57.2	14	4.4	573
CP6E4	Leucite Tephrite	≥ 574	359.6	67.2	14	3.5	574
CP6F1	Andesite	≥ 580	359.6	57.2	11	4.4	580
CP6H1	Leucite Tephrite	≥ 623	15.5	55.2	16	4.7	623
CP6I1	Leucite Tephrite	520*	29.9	66.7	11	13.1	603
CP6K2	Porphyritic Leucite Tephrite	≥ 601	346.5	44.6	15	4.7	601
CP6L1	Leucite Tuff	≥ 607	12.7	62.6	14	3.2	607
CP6M4	Porphyritic Leucite Tephrite	≥ 572	4.6	62.8	13	5.8	572
CP6N2	Leucite Tephrite	≥ 630	339.8	45.5	15	5.1	630
CP6O3	Porphyritic Leucite Tephrite	≥ 572	356.4	62.0	15	3.8	572
CP6Q3	Leucite Tephrite	≥ 548	0.7	49.5	12	3.3	548
CP6R1	Leucite Tephrite	≥ 609	2.6	40.9	16	6.5	609
CP6S3	Leucite Tephrite	≥ 571	359.4	61.6	16	4.4	571
CP6T2	Leucite Tephrite	≥ 533	344.7	61.2	13	3.1	533
CP6U3	Leucite Tephrite	≥ 587	43.2	56.7	12	2.9	587
CP6V1	Andesite	≥ 590	347.5	42.1	14	4.6	590
CP6W2B	Leucite Tephrite	≥ 553	348.4	53.3	11	4.2	553
CP6X2	Andesite	≥ 583	353.3	49.4	15	4.3	583
CP6Y1	Leucite Tephrite	520*	359.7	67.9	12	12.5	543

Symbols are the same as in Table 2.